Modelling heat transport in a High Temperature ATES system

A sensitivity study on the hydrogeological and operational parameters in High Temperature Aquifer Thermal Energy Storage systems controlling 1) the thermal impact on overlying layers and 2) the thermal recovery efficiency

Peter J.A. Oerlemans
MSc Thesis
Utrecht University – Faculty of Geosciences
February 2018

Supervisors:
1st: Prof. Dr. S.M. Hassanizadeh (Utrecht University)
2nd: Dr. N. Hartog (Utrecht University/KWR)
3rd: Ir. M. Bloemendal (KWR/ TU Delft)

Abstract

In order to create a sustainable planet, human kind has set ambitious goals to reduce CO_2 emissions in the near future. About 40% of the global energy consumption is used in heating and cooling in the built environment and the bulk of this energy is produced from fossil fuel burning. Aquifer Thermal Energy Storage (ATES) is a sustainable way for space heating and cooling. Surplus heat is stored in a subsurface groundwater aquifer during summer and reproduced in winter when heat demand is higher. Interest is aroused in High Temperature ATES (HT-ATES), where injection temperatures are higher (>25°C) than in regular ATES (<25°C). However, injection of warm water in a colder (~12°C) subsurface may thermally affect surrounding layers and induce processes that reduce the thermal recovery efficiency of the HT-ATES system. This research aims to find the processes and dominant hydrogeological and operational parameters controlling 1) the thermal effects of High Temperature ATES on overlying layers and 2) the thermal recovery efficiency of a HT-ATES system. To this end, and to provide more insight in the thermal transport in HT-ATES systems, a numerical 2D axisymmetric SEAWATv4 model was built to perform a sensitivity analysis around a reference Case Study scenario. The results showed that the thermal impact on an overlying aquifer mainly depends on the water injection temperature and the thickness of the cap layer that separates the overlying aquifer from the injection aquifer. The 1D steady state heat conduction theory provides an analytical solution that gives a good first order approximation of the nearly linear vertical temperature distribution in the overlying layers that can be expected on the long term. Density driven flow in the injection aquifer resulted in a larger radial extent of thermal impact on the overlying layers. Heat effects from the well casing was limited to locations close to the well. For low injection temperatures, heat conduction is the main process responsible for efficiency losses and optimizing the area over volume ratio increases the efficiency. At higher injection temperatures density driven flow also contributes to heat losses. For the modelled scenarios with higher injection temperatures, exceeding a critical injection aquifer thickness greatly increased density driven flow and decreased HT-ATES efficiency. Increasing yearly injection volume always benefits the efficiency of a HT-ATES system. These findings are valuable to identify under what conditions a secure and efficient realization of HT-ATES systems is possible.

KWR Watercycle Research Institute

Utrecht University

Contents

1 Introduction

Global greenhouse gas concentrations in the atmosphere have been rapidly increasing since the industrial revolution in the early 19th century. The measured global average temperature increase is 0.85 °C over the period 1880-2012 (IPCC, 2014). It is extremely likely that human activities and fossil fuel burning specifically are responsible for the bulk of the observed temperature increase (IPCC, 2007; IPCC 2014). The adoption of the Paris Agreement endorses the collective global ambition to limit global warming to +2°C with respect to pre-industrial times (UNFCCC, 2015). This means that fossil fuel burning must be reduced significantly. About 40% of the global energy consumption is used in heating and cooling in the built environment and the bulk of this energy is produced from fossil fuel burning (Omer, 2008; RHC, 2013). When heat and cold can be produced from sustainable sources, a significant reduction in greenhouse emissions can hence be achieved.

Aquifer Thermal Energy Storage (ATES) is a sustainable way for space heating and cooling and has achieved considerable energy savings already in the United States, Europe and other countries since the 1970s (Kim et al., 2010). ATES is used to overcome the seasonal discrepancy between availability and demand for heat, using the subsurface as a storage medium for thermal energy. Porous subsurface layers owe their suitability for this purpose to their low thermal conductivity, high heat capacity and large available space for storage.

ATES has high potential specifically in regions where both substantial seasonal variation in air temperature and favorable geohydrological conditions exist (Bloemendal et al., 2015). An example is the Netherlands, with a moderate maritime climate and many thick (unconsolidated) sedimentary aquifers present. Over 2000 ATES systems exist at shallow depth of 20-150 m.b.g.l. (Bloemendal & Hartog, 2018), with water temperatures of the warm and cold well in the range of 14-20°C and 5-12°C respectively (Sommer, 2015). In the Netherlands, heating and cooling in horticulture, industries and housing account for 40% of the total energy consumption, 90% of which is produced from fossil fuels (CE Delft, 2010). Moreover, the fossil energy used for heating is mainly derived from burning methane that is produced from the Groningen gas fields. National government has recently decided to strongly reduce the gas production as soon as possible because it induces earthquakes (Staatstoezicht op de Mijnen, 2018; van Bokkum, 2018). Other sustainable techniques are hence needed to support the Dutch heat demand. This emphasizes the potential for ATES systems to sustainably provide heat and cold in the near future.

Water from the cold ATES well can be used directly to cool buildings in summer but water from the warm well (<25°C) is not warm enough for direct heating and is, therefore, increased in temperature by a heat pump. Although helpful, the heat pump is relatively energy consuming, as it often accounts for over 50% of the total energy consumption of an ATES system (DWA, 2016). Another problem regarding ATES is that in Dutch cities scarcity of space occurs in the subsurface due to the popularity of these systems and other subsurface applications. Spatial planning has become more important at locations with a high demand for these systems to prevent mutual interaction.

High Temperature ATES

High Temperature ATES (HT-ATES) uses a higher injection temperature of the water (>25°C) and has come up as a potential solution to problems regarding energy consumption of the heat pump and scarcity of space in aquifers, as the heat pump employment is lower and less space is needed in the subsurface to store an equal amount of thermal energy. However, water with a higher temperature has a larger effect on the aquifer and its surroundings compared to lower injection temperatures. In the Netherlands, over half of the drinking water is produced from groundwater (Vewin, 2015). When temperatures of shallow drinking water aquifers are increased by underlying HT-ATES systems, the water quality may degrade. Additionally, higher injection temperatures increase density differences between injected and ambient waters. This results in buoyancy flow which in turn affects the thermal recovery efficiency of a HT-ATES system. More insight into the thermal transport and recovery

efficiency of HT-ATES systems is needed in order to identify under what conditions a widespread, secure and successful realization of HT-ATES is possible.

Scope
The processes initiated by HT-ATES can be of biological, chemical and physical nature. The focus of this research is on the physical processes related to heat transport in the injection aquifer and the layers overlying it. Specifically, the relative dominance of site-specific hydrogeological and operational parameters controlling 1) the thermal impact on overlying aquifers and 2) the thermal recovery efficiency of a HT-ATES system are investigated. The following research questions are set up to address the problem stated:

- Which effects of HT-ATES can be expected on overlying aquifers and what are the dominant hydrogeological and operational parameters controlling these?
- What are the dominant hydrogeological and operational parameters controlling thermal recovery efficiency of HT-ATES systems?
- What are the dominant processes responsible for energy losses in a HT-ATES system?
- What is the relative contribution of these processes to energy losses?

Approach
Theory is presented first to provide more insight in the heat transport processes playing in HT-ATES (Section 2.1). A general introduction to ATES is provided in 2.2. SEAWATv4 is a program capable of simulating 3D variable-density saturated groundwater flow and heat transport. It was used in this research to simulate heat transport in HT-ATES systems. A sensitivity analysis was performed to find the dominant parameters controlling efficiency and thermal impact of HT-ATES on overlying layers. The sensitivity analysis setup, assessment framework and model characteristics are described in sections 2.3 - 2.5. The recovered analytical and modelled results are then presented (section 3) and discussed (section 4) in light of the research targets. Finally, it is concluded what parameters and processes dominantly control 1) the thermal impact on overlying layers, and 2) thermal recovery efficiency of HT-ATES systems.

2 Methods and materials

2.1 Heat transport in the Subsurface

As advective upward transport of heat is inhibited by the confining layer, heat conduction is mainly responsible for the heating of layers overlying a HT-ATES injection aquifer and must hence be studied. According to Doughty et al (1982), the main processes causing energy losses in ATES are conduction, dispersion, regional groundwater flow and density driven flow. These heat transport processes and their impact in this research will be discussed in this section.

2.1.1 Heat Conduction

Heat conduction or thermal conduction is the transfer of heat (or internal energy) by microscopic collisions of particles within a body. The flux of heat quantifying conduction depends on the temperature gradient, which is the temperature difference over a certain distance interval, and the properties of the medium conduction occurs through. In HT-ATES, water is used as a medium to transport and store heat. As soon as warm water enters a subsurface with a lower temperature, heat conduction from the warm water to the surrounding material is initiated and will continue until temperature gradients are absent. The following subsections will discuss various aspects of heat conduction in a HT-ATES system.

2.1.1.1 Heat Conduction to upper layers

Aquifers overlying the injection aquifer with an aquitard separating them are safe from water mixing, but their temperature can increase by conduction through the aquitard (fig 2.1). An important

consideration for implementation of HT-ATES is how it affects the temperature of the surrounding aquifers. Thermally induced biological and chemical processes may negatively affect the water quality of the upper aquifer. Generally, it is assumed that these processes only moderately increase when temperature deviations are kept within 10°C with respect to the ambient temperature (Griebler et al., 2016). This study assumes that the water quality of the upper aquifer is getting negatively affected by the HT-ATES system when its temperature exceeds 25°C. This temperature is referred to as the critical temperature or T_{crit}. This study uses an ambient groundwater and soil temperature of 12°C. The bottom of the upper aquifer is referred to as the critical depth or D_{crit}. It is expected that biochemical and physical processes start affecting the quality of the upper aquifer when T_{crit} is measured at D_{crit}.

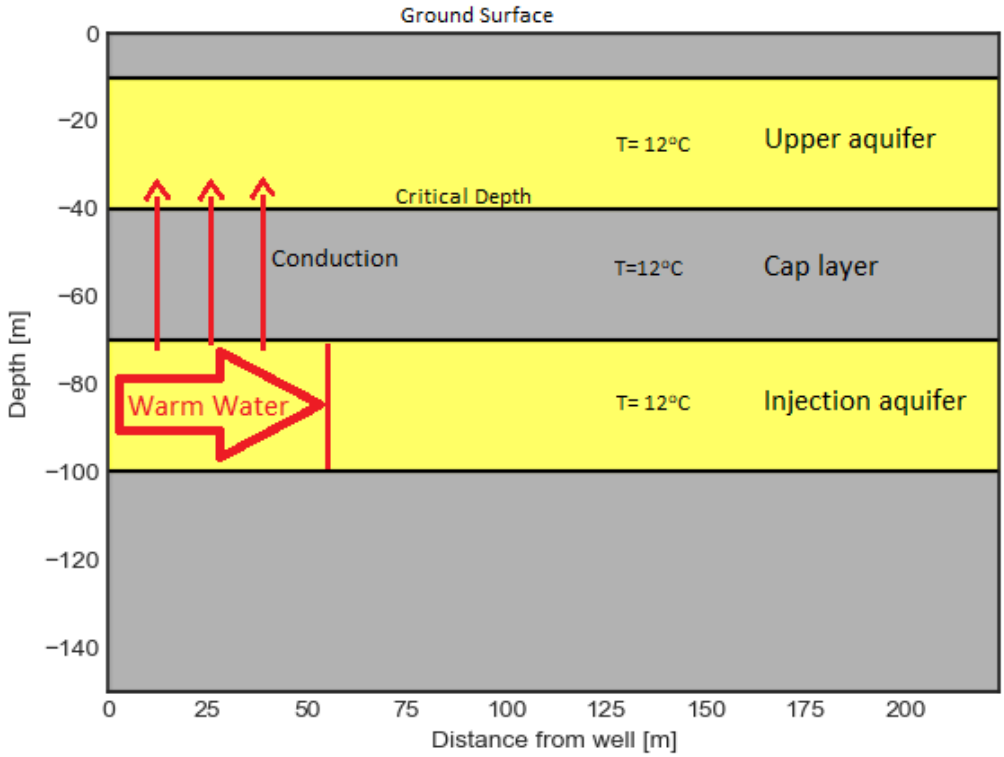

Figure 2.1. Schematic soil profile with aquifers (yellow) and aquitards (grey). Vertical red arrows indicate heat conduction from the injected warm water through the cap layer to the upper aquifer. The bottom of the upper aquifer is the critical depth and native soil temperature is 12°C.

The distinction between two modes of heat conduction is relevant here: steady state and transient heat conduction. Steady state heat conduction refers to the situation where the temperature distribution and heat fluxes in the system are constant in time. The system is said to be 'thermally stable' or 'in thermal equilibrium'. However, before this steady state situation is reached, transient heat conduction occurs meaning that temperatures and heat fluxes are changing in space and time. In transient heat conduction, the system moves towards the thermal equilibrium temperature distribution until the steady state situation is reached. The time needed before steady state conduction is obtained is called the equilibration time. The equilibration time can be large for systems with low thermal conductivities. Besides, when the heat capacity of the material is considerable i.e. when a lot of heat is needed to increase the temperature of a kg of soil by 1K, the movement of temperature front is lagged as it takes more energy hence time to heat a material to its equilibrium temperature. This results in slower movement of temperature fronts hence larger equilibration times. The following section provides the theory required to analytically derive the one-dimensional steady state temperature distribution in a vertical soil profile, given the subsurface properties and time-independent constant temperature boundary conditions at the top and bottom of the soil profile.

Steady state 1D Heat conduction

The one-dimensional form of Fourier's law of heat conduction is (Spakovszky, 2013):

$$q = -\lambda \frac{dT}{dx} \qquad \text{(E2.1)}$$

Or alternatively,

$$Q = -\lambda A \frac{dT}{dx} \qquad \text{(E2.2)}$$

with q the heat flux [W/m^2], Q the heat transfer rate [W], A the area [m^2] through which conduction occurs, λ the thermal conductivity [W/(m °C)] of the material and T [°C] and x [m] temperature and distance respectively. When the thermal gradient dT/dx is negative, the minus sign makes sure that heat flows in positive x direction. λ is temperature independent and homogeneous and isotropic for a layer of material.

Conduction of heat through a layer of material will occur down the temperature gradient i.e. from a hot to a colder location. Taking the temperatures of the boundaries of such a system constant, a steady state temperature distribution will be reached after a certain time. This means that there is going to be a constant heat flux q [W/m^2] along the temperature gradient, so that an equal amount of energy enters and leaves the considered system per unit time at its hot and cold side respectively. The total energy in the considered 1D system will then be constant.

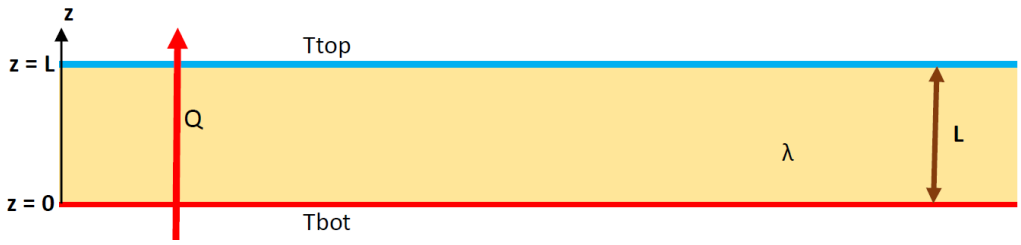

Figure 2.2. One layer of material through which steady state 1D conduction occurs. Q: heat transfer rate [W], L: thickness of layer [m], Ttop/Tbot: top and bottom constant temperature boundary conditions [°C], λ: thermal conductivity [W/m/K]. Q is constant in the spatial coordinate z.

For a one-layer system with two constant temperature boundaries and steady state one-dimensional heat conduction (figure 2.2), the temperature distribution is linear in z. the following expression for the heat transfer rate Q applies:

$$\mathrm{Q} = \frac{\mathrm{T}_{bot} - \mathrm{T}_{top}}{\mathrm{R}} \qquad \text{(E2.3)}$$

Where $\mathrm{R} = \frac{L}{\lambda \mathrm{A}}$ is the thermal resistance of the material [°C/W], defined by the length L [m] along the temperature gradient, the thermal conductivity λ and the conduction area A. The thermal resistance R increases with increasing L, and decreasing λ and A. T_{bot} and T_{top} are the temperature boundary conditions. Note that the minus sign of E2.2 has disappeared in E2.3 because dT = T_{top}-T_{bot} is negative as well. Notice that a low thermal conductivity and a high layer thickness L inhibit the transport of heat. In a one-layer system like figure 2.2, the temperature depends on the location only:

$$\mathrm{T(z)} = \mathrm{T_{bottom}} - \frac{\mathrm{T_{bottom}} - \mathrm{T_{top}}}{\mathrm{L}} * z \qquad \text{(E2.4)}$$

For a multi-layer system (figure 2.3), the heat flux by conduction is determined by the temperature difference over the considered system and the sum of the layer resistances. The total resistance is defined by the sum of the resistances of the different layers:

$$R = R_1 + R_2 + R_3 = \frac{L_1}{\lambda_1 A_1} + \frac{L_2}{\lambda_2 A_2} + \frac{L_3}{\lambda_3 A_3} \quad \text{(E2.5)}$$

Assuming that the area through which conduction occurs is constant, A can be taken out of the fractures. Combining E2.3 and E2.5 then gives:

$$Q = \frac{T_{bot} - T_{top}}{\frac{1}{A}\left(\frac{L_1}{\lambda_1} + \frac{L_2}{\lambda_2} + \frac{L_3}{\lambda_3}\right)} \quad \text{(E2.6)}$$

So that

$$q = \frac{Q}{A} = \frac{T_{bot} - T_{top}}{\frac{L_1}{\lambda_1} + \frac{L_2}{\lambda_2} + \frac{L_3}{\lambda_3}} \quad \text{(E2.7)}$$

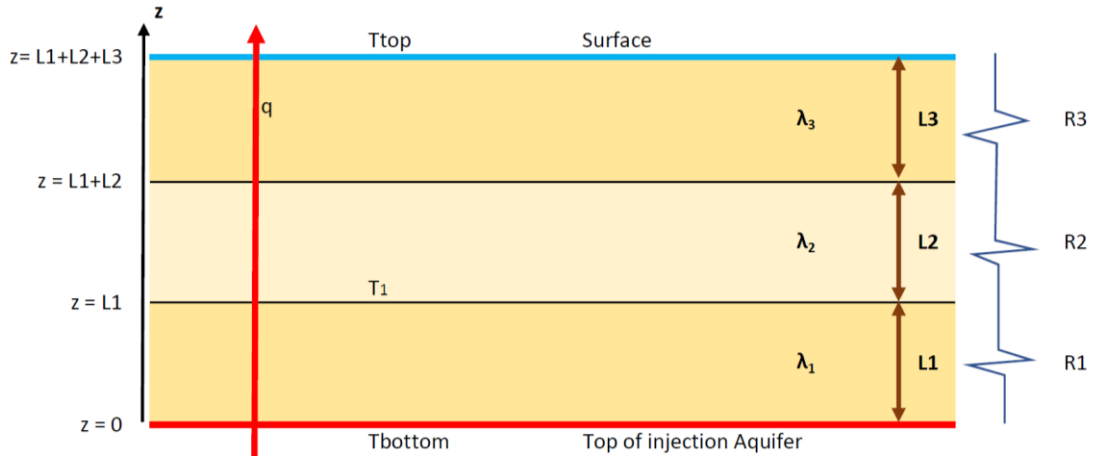

Figure 2.3. Multi-layered system with steady state 1D heat conduction. q: heat flux [W/m2], R: thermal resistance. Heat flux q is constant in z. T_1 represents the temperature at the top of the bottom layer L1. k represents thermal conductivity .

As for steady state 1D heat conduction, the heat flux q is constant along z, E2.7 can also be applied to the first layer only so that the temperature at the top of layer 1 (T_1) can be calculated:

$$q = \frac{T_{bot} - T_1}{\frac{L_1}{\lambda_1}} \rightarrow T_1 = T_{bot} - \frac{q * L_1}{\lambda_1} \quad \text{(E2.8)}$$

The multilayer steady state heat conduction theory is used to calculate the steady state temperature distribution in soil profiles, given the thermal conductivities (λ), thicknesses (L) and the temperatures at the boundaries. This research uses three layers overlying the injection aquifer, similar to figure 2.3. The hotter location is the injection aquifer and heat will be conducted from the top of this aquifer to the colder surface. It is assumed that no groundwater flow occurs, so heat is only transported by conduction. The expression for the steady state 1D conduction heat flux is then given by:

$$q_{tot} = q_{L1} \rightarrow \frac{T_{bot} - T_{top}}{\frac{L_1}{\lambda_1} + \frac{L_2}{\lambda_2} + \frac{L_3}{\lambda_3}} = \frac{T_{bot} - T_1}{\frac{L_1}{\lambda_1}} \quad \text{(E2.9)}$$

Solving for the temperature at the top of the first layer then the temperature at the critical depth, which is at the bottom of the upper aquifer:

$$T_1 = T_{bot} - \frac{\frac{L_1}{\lambda_1} * (T_{bot} - T_{top})}{\frac{L_1}{\lambda_1} + \frac{L_2}{\lambda_2} + \frac{L_3}{\lambda_3}} \quad \text{(E2.10)}$$

It is to be checked whether this analytical 1D model accurately represents the real situation.

2.1.1.2 Thermal equilibrium between solid and fluid

Upon injection, water continues to flow radially away from the well, but part of its heat is taken up by the aquifer sand particles, causing a retardation of the temperature front with respect to the water front. The retardation factor R_T (≥1) describes the extent of delay of the thermal front. It is made up of the aquifer properties porosity (θ) and the volumetric heat capacities (C_s and C_w) or the specific heat ($c_{p,s}$ and $c_{p,w}$) of the aquifer solid material and water respectively. Note that volumetric heat capacity is the product of specific heat and material density (ρ).

$$R_T = 1 + \frac{(1-\theta)}{\theta}\frac{C_s}{C_w} = 1 + \frac{(1-\theta)}{\theta}\frac{\rho_s}{\rho_w}\frac{c_{p,s}}{c_{p,w}} \quad \text{(E2.11)}$$

2.1.1.3 Shape of the storage volume

Typically, injection takes place in a confined aquifer, so that vertical flow through the top and bottom of the aquifer is negligible. Considering a fully penetrating well and disregarding density driven flow, the shape of the storage volume is a cylinder. The water injected is distributed radially over the pore spaces in the injection aquifer. The dimensions of the cylinder depends on the volume injected by the well (V_{in}) and the thickness (H) and porosity (θ) of the aquifer. From the mathematical expression of the volume of a cylinder ($V_{in} = H * \pi {R_H}^2$), the hydraulic radius R_H of the injected water cylinder in the soil can be deduced:

$$R_H = \sqrt{\frac{V_{in}}{\theta H \pi}} \quad \text{(E2.12)}$$

Due to thermal retardation, the radius of the thermal storage cylinder, i.e. the thermal radius (R_{th}), is smaller than the hydraulic radius (R_H):

$$R_{th} = \sqrt{\frac{V_{in}}{\theta H \pi R_T}} \quad \text{(E2.13)}$$

Figure 2.4 visualizes the shapes of the water and heat storage volumes, characterized by the hydraulic and thermal radius respectively.

Since conduction occurs through the outer surface of the thermal cylinder, the lowest heat losses by conduction can be obtained by minimizing it with respect its volume i.e. by finding the lowest value of Area/Volume ratio for a given ATES configuration. The cylinder has two circular areas at its top and bottom and one outer plane. Following Doughty et al. (1982) the A/V ratio of the thermal storage cylinder is defined by the filter length (L) and the thermal radius R_{th}:

$$\frac{A}{V_{in}} = \frac{2\pi R_{th}^2 + 2\pi R_{th} L}{\pi R_{th}^2 L} = \frac{2}{L} + \frac{2}{R_{th}} \quad \text{(E2.14)}$$

For a given injection volume, the optimal filter length can be found. Note that for this study the filter length is equal to the injection aquifer thickness, because this study uses fully penetrating wells. Figure 2.5a shows the dependency of A/V of filter length L for a given injection volume. The sensitivity of A/V to L is higher for lower storage volumes, and when L is small. The shape of a storage cylinder can also be expressed as the ratio of its height and the radius of the thermal volume: L/R_{th}. Doughty (1982) found that the optimal L/R_{th} ratio is around 1.5 for systems excluding groundwater flow and density driven flow.

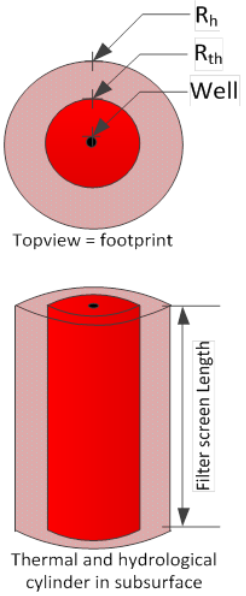

Figure 2.4. Top view (above) and sideview (below) of Hydraulic radius R_h (pink), Thermal radius R_{th} (red) and well (black dot) (after Bloemendal & Hartog, 2018) .

Simulation studies performed by Doughty et al (1982), Lopik (2016) and Bloemendal & Hartog (2018) all showed that the relation between thermal recovery efficiency and A/V ratio is linear when density dependent flow is negligible and when no background groundwater flow occurs (see figure 2.5b).

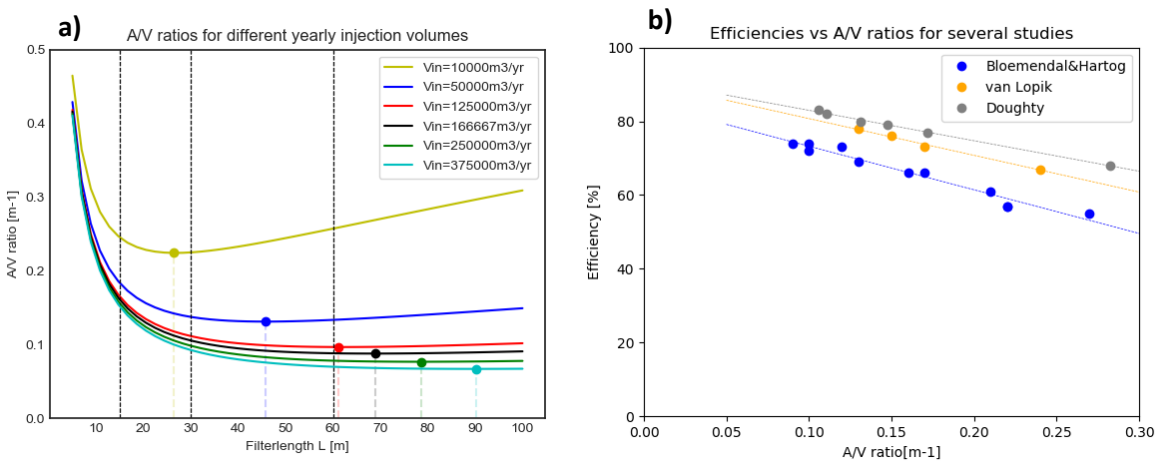

Figure 2.5. a) A/V ratio of cylindrical water storage volumes with filter screen length, for several injection volumes. b) efficiencies plotted versus A/V ratio for simulation studies where no buoyancy flow and regional groundwater flow is considered (Doughty, 1982; van Lopik, 2015; Bloemendal & Hartog, 2018)

2.1.1.4 Conduction and dispersion at the thermal interface

In ATES systems, the injected heat is primarily moved by advection (flow) induced by pumping activity. The boundary between the hot storage cylinder and the colder ambient groundwater (also called the interface) may spread because of mechanical dispersion and heat conduction. Molecular diffusion is negligible with respect to the flow induced by pumping. The mechanical dispersion spreads the heat over the interface due to velocity and path variations of the water particles in the soil with respect to the average pore velocity and flow direction of the thermal front. The heat transport process of thermal conduction is mathematically similar to molecular diffusion of solutes (Langevin et al., 2007), but instead of a molecular diffusion coefficient [L^2/T] used for solute transport, in heat transport a thermal conduction term is used, which is known as the bulk thermal diffusivity [L^2/T]. For soils, this thermal diffusivity (~10^{-6} m^2/s) is a couple of orders of magnitude larger than the molecular diffusion coefficient (~10^{-10} m^2/s), so that the latter process can be neglected. The processes of thermal conduction and dispersion remain to be considered for spreading heat across the thermal interface. Their combined effect is described using the effective thermal dispersion, which comprises the bulk thermal diffusivity and the thermal dispersion term (Bloemendal & Hartog, 2018):

$$D_{eff} = \frac{\lambda_{aq}}{\theta \rho C_w} + \frac{\alpha v}{\theta} \qquad \text{(E2.15)}$$

With D_{eff} the effective thermal dispersion. The diffusivity term is represented by the bulk thermal conductivity of the aquifer λ_{aq} and by θ, ρ and C_w, which are the porosity, water density and volumetric heat capacity of water respectively. The mechanical dispersion term contains the dispersivity of the aquifer α [m], the pore velocity v [m/s] of the water and the porosity θ. The rate of conduction is expressed using the increasing standard deviation, giving the distance covered by a thermal front for a given time, in semi-infinite space

$$\sigma = \sqrt{2 D_{eff} t} \qquad \text{(E2.16)}$$

Mechanical dispersion and conduction are important processes for heat losses at the boundary of the stored thermal energy body. Therefore, the geometric shape of the storage volume is important, as this defines the area of boundary available for these processes to occur.

The relative importance of dispersion and conduction at the interface depend on the (flow) conditions (see equation D_{eff}). Close to the well, flow velocity is high and dispersion accounts primarily for the spreading of the interface. Further away from the well, flow velocity hence the thermal dispersion term declines and the conduction term starts controlling the spreading of the interface. Bloemendal &

Hartog (2017) showed that for the range of system configurations in the Netherlands, conduction theoretically dominates in the dispersivity equation already after 10% of the total yearly water volume is injected, even for relatively high dispersivity values (figure 2.6). This means that conduction also dominates when the targeted volume is injected. They also found that dispersion losses that occur close to the well are overtaken by the advective heat transport when injection continues, so that the interface is rather sharp towards the end of the injection period. This sharp interface is not spreading because of conduction, since the injected heat moved faster than the heat transport by conduction ($\sigma = \sqrt{2D_{eff}t}$) in the most of their ATES configurations and operations. When injection stops, the interface starts spreading by conduction. Upon extraction, the interface will spread considerably, because of the opposite effects of these processes. The heat that is not recovered helps improving the recovery efficiency over multiple cycles, as less heating of the aquifer material occurs the next cycle.

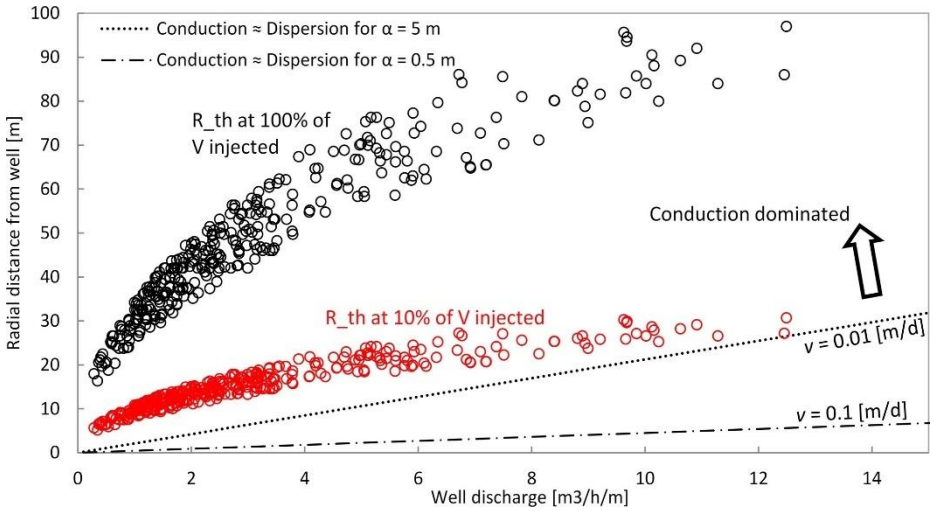

Figure 2.6. Lines indicate the relation between specific well discharge and radial distance from the well where conduction and dispersion of the interface is equal (E2.16). Open circles represent the radial distance from the well of the thermal front with respect to the specific well discharge after 10% (red) and 100%(black) of the injection volume is injected (Bloemendal & Hartog 2018).

2.1.2 Regional groundwater displacement

Another process affecting the thermal recovery efficiency is regional groundwater flow (or background flow). When a natural hydraulic gradient exists that is capable of moving the thermal energy body within the time scale of one cycle, the injected water body as a whole will be displaced down the gradient. Thermal energy leaving the range of the well is considered lost. Bloemendal and Hartog (2018) showed that loss of thermal recovery efficiency due to displacement is dominant for ATES systems where $R_{th}/u < 1$ [y] i.e. where the value of the thermal radius R_{th} [m] is smaller than the value for regional groundwater flow u [m/y]. In this study background flow is neglected.

2.1.3 Density driven flow

Density driven flow, also called buoyancy flow or free convection, is flow that is induced by temperature-induced density differences between water bodies in contact with each other. A body of water with a lower density than the surrounding water tends to move upwards by buoyancy (see flow field in figure 2.7), towards an equilibrium situation. In HT-ATES, the injected water is warmer hence lighter than the ambient groundwater and tends to move upwards and spread over the cap of the aquifer. Consequently, a part of the injected warm water is left within the aquifer after the production period. Simultaneously, denser colder water moves under the injected warmer water at the bottom of the aquifer. Because cold water is produced at the bottom of the well screen, the process of density driven flow can contribute to considerable heat losses of HT-ATES systems. The rotation of the interface induces a change of the geometric shape of the storage volume from a cylinder to a conical shape. This in turn influences the conduction losses, as the area at the top of the thermal volume is

larger than the area at the bottom, and the A/V ratio increases. So the losses by conduction are also dependent of the extent by which density driven flow changes the thermal storage shape. The decrease in viscosity with temperature is another important factor facilitating flow as resistance to flow decreases with temperature.

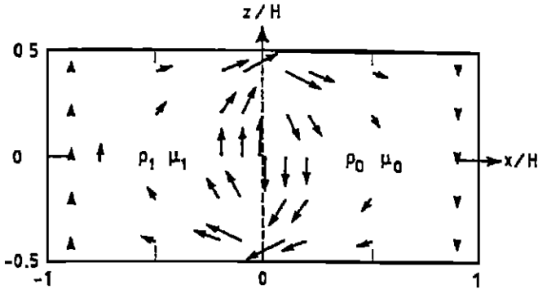

Figure 2.7. Vertical cross section through an infinite aquifer layer with thickness H, showing the flow field around the interface (vertical dashed line) for a situation with buoyancy flow only (after Hellstrom et al., 1988a). *Viscosities: μ, fluid densities: $\rho_0 > \rho_1$.*

To allow for quantification of buoyancy flow, theory on density driven flow and interface rotation in both Aquifer Storage and Recovery (ASR) and HT-ATES are presented.

2.1.3.1 Mixed convection ratio

Ward et al. (2007) studied the significance of density dependent flow and transport in ASR systems, where buoyancy flow occurs because of salinity-induced density differences. Ward showed in what range density driven flow becomes relevant and what parameters determine its importance. Viscosity effects on flow were neglected and a sharp fresh-saline water interface was assumed.

Advective transport of heat is also called convection. Two types of convection exist in a groundwater system where HT-ATES is applied: forced convection and free convection. Forced convection is caused by a hydraulic gradient e.g. by pumping activities or a regional hydraulic gradient. When forcing occurs because of pumping only, convection at the interface is defined as the flow velocity v_{forced} [m/d] at a radius r [m] of the interface from the well with discharge Q [m^3/d] in an aquifer with thickness H [m] and porosity θ [-], assuming that injection takes place in a homogeneous and isotropic aquifer:

$$v_{forced} = \frac{Q}{2\pi r \theta H} \qquad \text{(E2.17)}$$

Free convection here refers to buoyancy flow caused by a density gradient e.g. due to differences in injected water and ambient aquifer water. It is defined by the hydraulic conductivity k [m/d], porosity θ [-] of the aquifer and the density difference ratio α [-] of the two water bodies.

$$v_{free} = \frac{k\alpha}{\theta} \qquad \text{(E2.18)}$$

$$\text{with } \alpha = \frac{\rho_f - \rho_{f,0}}{\rho_{f,0}} \qquad \text{(E2.19)}$$

where ρ_f and $\rho_{f,0}$ represent the density [kg/m^3] of the injected and ambient water respectively. Together, forced convection (acting in horizontal direction) and free convection (acting in vertical direction) make up the overall flow and transport regime. Ward et al. presented a mixed convection ratio M of the free and forced convection. It states the relative importance of the convection types given certain aquifer and operational parameters and is defined as follows:

$$M = \frac{v_{free}}{v_{forced}} = \frac{2\pi r H}{Q} k\alpha \qquad \text{(E2.20)}$$

Values for M close to 1 indicate that forced and free convection balance. If M<<1 the forced convection dominates the flow in the system and for M>1 free convection is dominant (see figure 2.8)

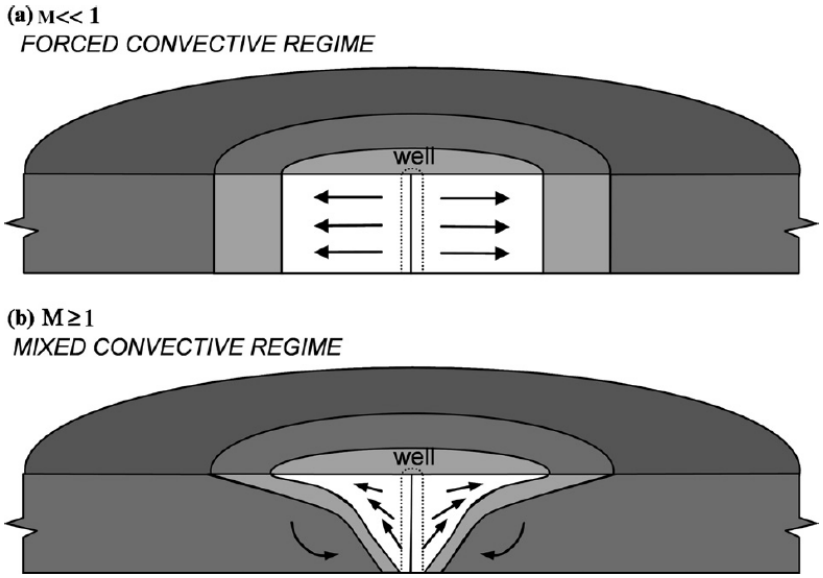

Figure 2.8. Schematic of two convective regimes. a) forced convection dominates free convection, so that tilting of the fresh-salt interface is limited. b) forced and free convection have similar magnitude, giving a mixed convection regime. (Ward et al., 2007)

For limited differences in salinity, dynamic viscosity differences are small in ASR systems and the theory of Ward is applicable to these systems. But since viscosity is more sensitive to temperature, it is an important factor facilitating flow in HT-ATES and the impact of temperature driven buoyancy flow in HT-ATES systems is underestimated by the method of Ward. In later work, Ward et al. (2008, 2009) developed a more extended and empirical framework for characterizing the flow dominance in ASR systems, but their extensive expression has no added value to this particular research.

2.1.3.2 Analytical solution for the interface movement in ASR

Bakker (2010) derived an analytical expression for the movement of the interface between native brackish and injected fresh water in ASR systems. Bakker assumed Dupuit flow for ASR systems in confined homogeneous and horizontal aquifers and neglected viscosity variability and dispersion of the interface. The pumping scheme is a block function with consecutive phases of injection, storage, production and rest. His research showed that the radial velocities of points on the interface are only a function of time, the vertical coordinate and a dimensionless parameter D, which is defined by the discharge of the well [m^3/d], the hydraulic conductivity k, the aquifer thickness H and the dimensionless density difference α (as E2.19) between the water bodies:

$$D = \frac{Q}{k\alpha H^2} \qquad \text{(E2.21)}$$

Bakker showed that larger values of D resulted in higher efficiencies. Numerical calculations executed by Bakker (2010) support this relation. Efficiency is independent of the actual period of the four phases, only dependent on their relative lengths. In Bakkers freshwater recovery efficiency calculation, extraction of water stops when native saline water reached the bottom of the well. According to Bakker then, efficiency is defined as the volume of extracted (fresh) water over the total volume injected, so $V_{in} \neq V_{out}$. This means the volume of the freshwater produced determines the efficiency, rather than the quality (concentration) of the water produced. This is a different way of calculating the efficiency compared to this study, where $V_{in}=V_{out}$ and where efficiency is defined by the ratio of

produced and injected heat. Because of the different definition, efficiency defined by Bakker cannot be compared to the thermal recovery efficiency used in HT-ATES systems. However, the fact that efficiency is accurately described by D gives qualitative insight in the key parameters contributing to density driven flow.

2.1.3.3 Validation of methods of Ward and Bakker by field data

Zuurbier et al. (2013) used the method of Ward (R_{ASR}) and Bakker (D) to estimate the performance of ASR systems with fully penetrating wells in a Dutch coastal area. They found a good agreement between the data and the results from the theoretical methods, for limited hydraulic conductivity anisotropy ratios ($k_h/k_v < 3$). Despite the fact that the method of Bakker does not consider lateral flow, anisotropy and mixing of the different waters, the predicted recovery efficiencies matched the data (9 cases) quite well. Underestimations of some cases can be caused by the fact that anisotropy is not incorporated in this method. For the method of Ward et al. (2009) they found that ASR systems were expected to perform well for $R_{ASR} < 0.1$. Although no definition for recovery efficiency was included in this method, its capability of incorporating anisotropy payed off when accurate anisotropy data was available. This indicates that anisotropy (i.e. when $k_v < k_h$), is a considerable factor controlling the extent of free convection. D comprises similar parameters as M, but in D the aquifer height H is squared and therefore more determinant in the definition of D, whereas the radius is used in the definition of M.

2.1.3.4 Tilting of a thermal front

Hellstrom et al. (1988b) performed an analytical study to the combined forced convection and buoyancy flow at the interface between hot injected water and colder native water. Their findings are valid for planar and cylindrical interface cases. They disregarded heat conduction through and dispersion of the interface, so that the thermal front was assumed to be rather sharp. They made a distinction in two types of tilting flow: 1) buoyancy tilting flow induced by density differences between the fluids and 2) forced convection that moves the interface laterally and simultaneously induces additional tilting flow because of a difference in viscosity. These two types of tilting depend on the tilting angle (α), the viscosity ratio of ambient and injected water ($\frac{\mu_0}{\mu 1}$) and the anisotropy parameter of aquifer permeability ($\sqrt{\kappa_v/\kappa_h}$). Additionally, the buoyancy flow increases with the thickness H of the aquifer and the density difference between the water bodies. The forced convection is also defined by the forced convection flow rate, caused by pumping. The tilting rate of the interface depends mainly on the temperature, as it controls the density and the viscosity of the liquids hence their behavior. So for the reference scenarios with equal discharge but different injection temperatures, the tilting angle is expected to be larger at larger injection temperatures.

For a situation with buoyancy flow only (see flow field in fig 2.7), Doughty et al. (1982) simplified the formulas of Hellstrom et al. (1979) and expressed the characteristic tilting time t_0 it takes for an initially sharp vertical interface to rotate 60 degrees, see E2.22. This is applicable if no pumping occurs i.e. when the thermal volume is just stored in the aquifer. If t_0 is larger than the storage time of the ATES operation, the tilting is expected to be moderate.

$$t_0 = 0.034 * \frac{H}{\sqrt{\kappa_v \kappa_h}} * \frac{C_a}{C_w} * \frac{\mu_0+\mu_1}{\rho_0-\rho_1} \qquad \text{(E2.22)}$$

With C_a and C_w the volumetric heat capacities of the aquifer [J/(m^3 K)] and the water respectively. κ_v and κ_h represent the vertical and horizontal permeability [m^2/s] respectively. Note that permeability (κ) and hydraulic conductivity (k) are related to each other by the fluid viscosity (μ) and density (ρ) of the native (subscript 0) and injected water (subscript 1), and the acceleration by gravity (g) [m/s^2]:

$$\kappa = k\frac{\mu}{\rho g} \qquad \text{(E2.23)}$$

The characteristic tilting times can be calculated for various scenarios. It is to be checked whether it provides a trustable first order approximation of the extent of buoyancy flow to be expected.

Adding forced convection to the situation, the thermal front is moved laterally (figure 2.9.a). When the thermal front is tilted, there is a lower flow resistance hence more flow in the warmer part of the aquifer because of the lower viscosity of warm water. Consequently, forced convection not only moves the interface laterally, it also enhances the tilting rate during injection of warm water (fig 2.9.b) and decreases it during production.

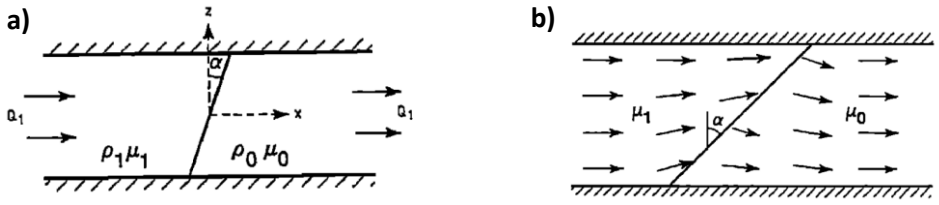

Figure 2.9. vertical cross sections through an infinite confined aquifer layer with thickness H. Viscosities: $\mu_0 > \mu_1$, fluid densities: $\rho_0 > \rho_1$, tilting angle w.r.t. vertical: α. a) hot (left of interface) and cold (right of interface) fluids separated by sharp tilted interface. b) forced convection flow field in an aquifer with tilted thermal front. The difference in fluid viscosity results in a non-uniform flow field. After Hellström et al. 1988b).

Depending on the situation, a certain stable tilting angle α_s from the vertical may exist, where the buoyancy and forced convection flow balance and the front is stable. The stable tilting angle increases with layer thickness (H) and injection temperature and decreases when more forced convection occurs. Hellström found that the tilting angle converges to α_s if $Q_1 * (\mu_0 - \mu_1) < 0$, and diverges away from α_s if $Q_1 * (\mu_0 - \mu_1) > 0$. In these expressions, Q_1 is the forced convection flow rate per unit horizontal width of the thermal front [m^2/s], which is positive during injection and negative during production (Hellstrom et al., 1988, b). $\mu_0 - \mu_1$ is always positive, so that theoretically the interface rotates away from α_s upon injection (i.e. when $Q_1>0$), and moves towards α_s during production (i.e. when $Q_1<0$). Based on this theory, it can be expected that the tilting angle oscillates during a cycle. It diverges from and converges to the stable angle upon extraction and production respectively. Note that this research considers cylindrical storage, meaning that the flow velocity of the interface is smaller at larger distance from the well. Consequently, buoyancy flow is expected to become relatively important towards the end of injection and the beginning of production period. Calculations on the stable tilting angle are not expected to provide trustable and representative insights, because both the flow velocity and tilting angle of the thermal front are variable in time because of the cylindrical storage. Another process complicating the calculations is heat conduction, which diffuses the interface between the injected and native water, especially towards the end of the injection period when advective heat transport is lower. According to Hellström and Doughty, a diffuse thermal front results in a slightly lower tilting rate.

2.2 Aquifer Thermal Energy Storage (ATES)

2.2.1 Classification and Configuration of Thermal Energy Storage systems

A classification of geothermal energy systems is provided in figure 2.10. Underground Thermal Energy Storage (UTES) is the more general term used for applications using the subsurface to store energy. The technique uses the low soil thermal conductivity to efficiently store heat during a season. Energy savings up to 80% for space cooling and 30% for space heating can be achieved (Schout et al., 2014). The two most commonly used types of UTES are Aquifer Thermal Energy Storage (ATES) (figure 2.11A) and Borehole Thermal Energy Storage (BTES) (figure 2.11B). BTES is a closed loop system: a fluid is circulated through the loop and heat exchange by conduction between the pumped fluid and the surrounding soil material provides the heat or cold needed. This technique is suitable for limited heat and cold demands like individual houses. An ATES system is open, meaning that the groundwater is used to transport thermal energy to and from the aquifer, where it is stored within the water and sand particles. It has a larger heat and cold supplying potential than BTES. With over 2000 ATES systems

operating by the end of 2015 (Economische Zaken, 2016), the Netherlands is a leading country applying ATES, mainly using low temperatures <25°C (Cabeza, 2015) in a doublet well configuration (figure 2.11A). In doublets, the hot and cold well screens are located in the same aquifer, at approximately equal depth but at a certain distance to each other to prevent negative mutual influence (Bloemendal et al., 2015). According to the Water Act, the maximum water infiltration temperature in the Netherlands is 25°C. Interest is aroused in storing water at higher temperatures using similar system configurations. Therefore, the terms Low Temperature ATES (LT-ATES) and High Temperature ATES (HT-ATES) are used in this research to refer to ATES with water injection temperatures of <25ºC and >25ºC respectively.

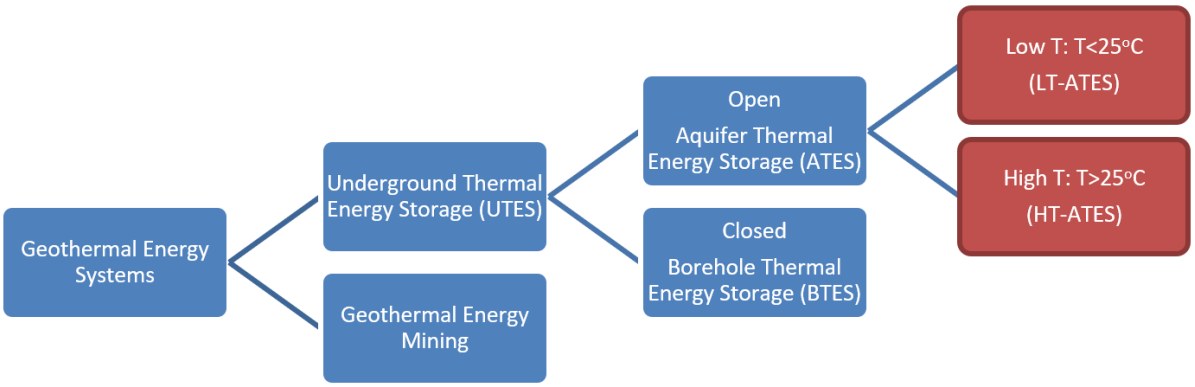

Figure 2.10. A classification of geothermal energy systems based on their purpose: either storing or producing heat. The low temperature ATES systems are most common in the Netherlands. The red boxes are the systems focused on in this research.

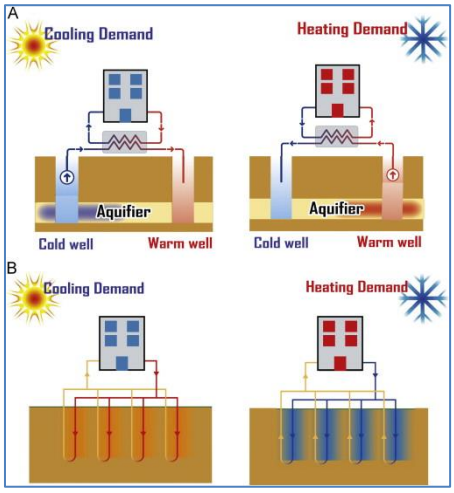

Figure 2.11. Two UTES system configurations with arrows indicating flow direction during operation in summer (left) and winter (right). A) Doublet ATES system configuration, B) BTES system configuration. (After Lim, 2013)

2.2.2 Thermal Recovery Efficiency

The thermal recovery efficiency is the primary parameter defining the total energy savings realized by an ATES system. It is defined as the heat recovered over the heat injected. The definition of thermal recovery efficiency includes the injected and produced water volumes and their corresponding temperatures in time.

$$\eta_{th} = \frac{E_{ex}}{E_{in}} = \frac{\int_{t_{start}}^{t_{end}} Q_{ex} * (T_{ex} - T_a) * C_{p,w} * \rho_w \, dt}{\int_{t_{start}}^{t_{end}} Q_{in} * (T_{in} - T_a) * C_{p,w} * \rho_w \, dt} \qquad \text{(E2.24)}$$

With η_{th} the thermal energy recovery efficiency, $E_{ex/in}$ [J] the thermal energy during extraction/injection, t_{start} and t_{end} [s] the start and end of the period over which efficiency is calculated

(one complete cycle); $Q_{ex/in}$ the average extracted/injected water volume over time interval dt [s], ($T_{ex/in}$-T_a) the temperature difference [°C] between the extracted/injected water ($T_{ex/in}$) and the ambient groundwater (T_a), $C_{p,w}$ the specific heat of water [J/kg/°C] and ρ_w [kg/m^3] the density of the water. The sensitivity of specific heat to temperature is negligible for the temperature range considered and therefore $C_{p,w}$ is taken constant so that it falls out of the equation. Also, hand calculations show that the density ratio of the produced and injected water ($\frac{\rho_w(T_{ex})}{\rho_w(T_{in})}$) is 1.02 for an extremely negative scenario of injection of 80°C water and average production of only 40°C water. Explorative model simulations show that produced temperatures will be higher so that the ratio will be even closer to 1. Therefore, it is justified to take a constant density value at both sides of the fracture, so that final expression for the thermal recovery efficiency of a cycle becomes:

$$\eta_{th} = \frac{E_{ex}}{E_{in}} = \frac{\int_{t_{start}}^{t_{end}} Q_{ex}*(T_{ex}-T_a)\,dt}{\int_{t_{start}}^{t_{end}} Q_{in}*(T_{in}-T_a)\,dt} = \frac{\sum_{t=t_{start\_cycle}}^{t=t_{end\_cycle}} Q_{ex}(t)*(T_{ex}(t)-T_a)*dt}{E_{in}} \qquad \text{(E2.25)}$$

The reference temperature is the ambient groundwater temperature. When a lower reference temperature is used, this also affects the efficiency of the system. Because $T_{ex} < T_{in}$ (because of heat losses), lower values for T_a result in higher ratios of $\frac{(T_{ex}-T_a)}{(T_{in}-T_a)}$ hence higher efficiencies. This is because the temperature difference between injected and extracted groundwater then becomes smaller relative to the reference temperature. For this study the average groundwater temperature of 12°C will be used as the reference temperature. The total yearly injection and extraction volumes are equal ($V_{in}=V_{out}$ and $\sum Q_{in} = \sum Q_{out}$), allowing for reliable comparison of the simulation results. Also a constant injection temperature is applied, leaving the extracted water temperature the time-dependent variable controlling thermal recovery efficiency.

2.2.2.1 Thermal Recovery Efficiency independent of injection temperature

Consider a case where density driven flow and regional groundwater flow are negligible. Higher injection temperatures result in higher absolute heat losses, but since more heat energy is injected as well in an equal proportion, the resulting thermal recovery efficiency does not change. Kranz & Bartels (2009) showed that the relation between the recovery efficiency of an ATES doublet system and the injection temperature depends on the relation of the produced temperature at the cold well with respect to the ambient aquifer temperature. This is valid for homogeneous aquifers without density driven and regional groundwater flow and when equal injection/extraction volumes and cycle lengths apply. One can take the temperature at the cold well equal to the ambient groundwater temperature. By doing so, the recovery efficiency is essentially calculated with respect to the groundwater temperature. This is also done in this research. Analytical analysis shows that in this case, the thermal energy recovery is independent of the injection temperature at the warm well. Their numerical results supported this (see figure 2.12, horizontal line). Exploratory modelling with the model used in this study also showed that efficiency is equal when different injection temperatures are taken, when the same assumptions from Kranz & Bartels apply.

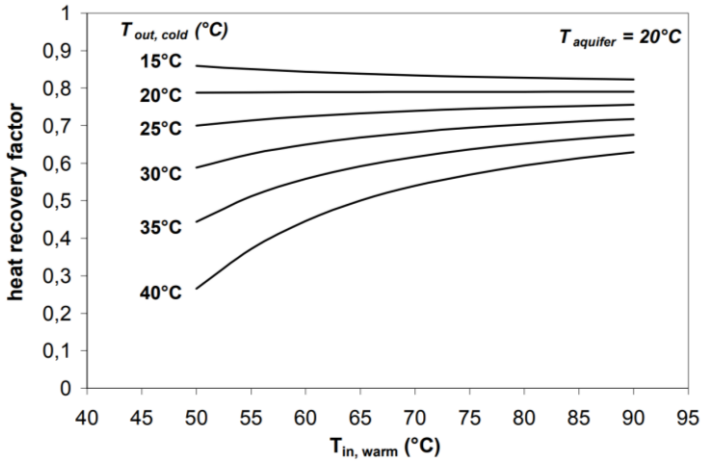

Figure 2.12. Effect of injection temperature at warm well ($T_{in,warm}$) on the thermal recovery efficiency (in fractions) for different cold well production temperature ($T_{out,cold}$) scenarios and for an aquifer temperature of 20°C. Efficiency is constant with $T_{in,warm}$ when $T_{out,cold}$=$T_{aquifer}$ (20°C). After Kranz & Bartels (2009).

2.3 Sensitivity Analysis

A sensitivity analysis was performed by simulation of several scenarios with SEAWATv4, to see what hydrogeological and operational parameters dominantly control 1) the heating of the upper aquifer and 2) the thermal recovery efficiency of the system. The reference scenario is presented first, followed by the other scenarios simulated.

2.3.1 Reference scenario: Case Study Koppert-Cress

Koppert-Cress (KC) is a horticulture business interested in HT-ATES. It is located in the Westland municipality in Zuid-Holland, the Netherlands. The Province of Zuid-Holland closed a 'green deal' with KC, permitting them to inject water up to 45°C. The company already has a LT-ATES system in use, but in this pilot project the installation is transformed into a HT-ATES system. In order to obtain operational guidelines for the new system, insight in the transport of injected water and heat is required. The sensitivity analysis was performed around a reference scenario that is based on the Koppert-Cress HT-ATES configuration. This scenario comprises the upper five lithological layers, alternating between clay and sand (see table 2.1).

Table 2.1 Lithology of the reference scenario used in this study, with hydrogeological and thermal properties. Colors indicate lithology: grey: clay, yellow: sand. H: layer thickness, zBot: depth of bottom of layer, k_H and k_V: horizontal and vertical hydraulic conductivity respectively, Θ: porosity, ss: specific storage, λ: bulk thermal conductivity of the layer, $C_{p,solid}$: specific heat of the solid grains; ρ_{bulk}: bulk soil density .

Layer no. [-]	Soil type [-]	H [m]	zBot [m]	k_H [m/d]	k_V [m/d]	Θ [-]	ss [m^{-1}]	λ [W m^{-1} K^{-1}]	$C_{p,solid}$ [J kg^{-1} K^{-1}]	ρ_{bulk} [kg m^{-3}]
1	clay	10	-10	0.05	0.01	0.3	1E-5	2.5	1500	1800
2	sand	30	-40	20.00	4.00	0.3	1E-5	2.5	710	2148
3	clay	30	-70	0.05	0.01	0.3	1E-5	2.5	1500	1800
4	sand	30	-100	20.00	4.00	0.3	1E-5	2.5	710	2148
5	clay	50	-150	0.05	0.01	0.3	1E-5	2.5	1500	1800

Layer 2, 3 and 4 are referred to as the upper aquifer, cap/clay layer and the injection aquifer respectively. The term 'reference scenario' applies to a scenario with lithological, hydrogeological and thermal soil properties as shown in table 2.1 that injects and produces 250,000m^3 of warm water each year (yearly discharge Q_y = 250,000 m^3/yr), using a Sine pumping scheme (figure 2.13a). Other studies

also used blocked functions (figure 2.13b) to describe the pumping activity, but the sinusoidal scheme was expected to best describe the yearly heat supply and demand (peak in heat supply and demand in summer and winter respectively). The reference scenario assumes a fully penetrating well configuration, meaning that the filter is screened from the top to the bottom of the injection aquifer. Heating from the well casing is not included in the reference scenario, but density driven flow and viscosity variations are. The well configuration is a doublet system in a relatively shallow aquifer, where the injected water temperature (T_{inj}) is higher than the ambient groundwater temperature of 12°C. Only the warm well will be considered since the research effort is concentrated around the heat transport processes occurring in and around the warm well. By taking the temperature of the cold well equal to the ambient groundwater temperature, the thermal recovery efficiency is calculated with respect to the groundwater temperature (see theory Kranz & Bartels, 2009). The ambient groundwater has a temperature is 12°C and a zero solute concentration .

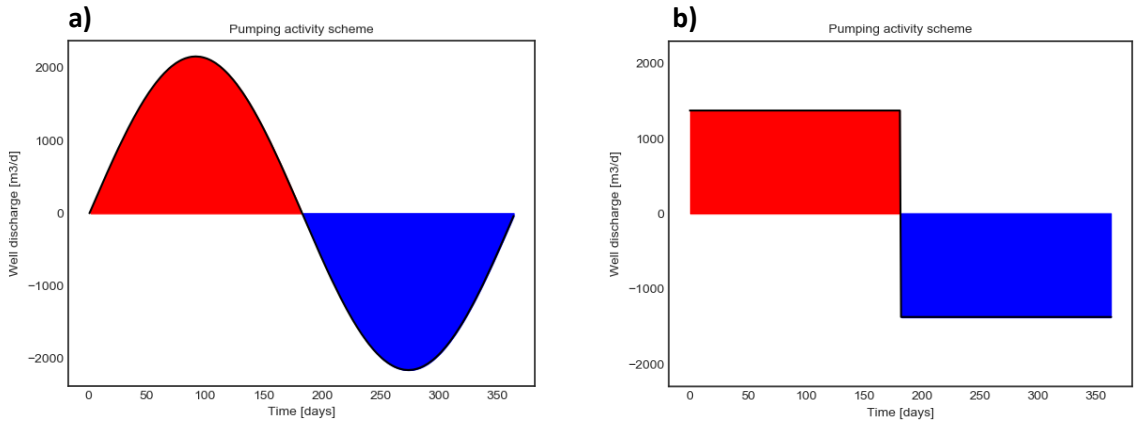

Figure 2.13 Pumping schemes of the warm well, showing the well discharge course during one cycle of 360 days, starting at the beginning of a warm season (e.g. spring). Red and blue colors indicate warm water injection and production respectively. a) Sinusoidal function, used for this study b) blocked function.

2.3.2 Scenarios

The sensitivity analysis matrix shows the properties of the scenarios simulated by SEAWATv4 and is presented in table 2.2. The range of the parameters used are assumed to be reasonable for the typical ATES systems in use in the Netherlands. The green row represents the Reference scenario. Other rows show the simulated scenarios and their properties. The complete sensitivity analysis was executed four times for four different injection temperatures of 20, 40, 60 and 80°C. Given the injection temperature T_{inj}, the sensitivity analysis was performed by subsequently varying one parameter (shown in orange in the figure) by a factor dfact with respect to the reference input. A parameter to be adjusted in the sensitivity analysis can be of operational or hydrogeological nature. For each injection temperature the dominant parameters controlling thermal impact on upper layers and efficiency can be found.

The parameters to be varied in the sensitivity analysis are sc1: the thickness of the cap layer H_{cap} (layer 3 in table 2.1), sc2: the thickness of the injection aquifer H_{inj} (layer 4 in table 2.1), sc3: the vertical hydraulic conductivity of sand layers (k_v) and sc4: the yearly injected/extracted volume (Q_y). An additional scenario (sc5) is performed where heating from the well casing is included to see its thermal impact on the surroundings. To see the effects of density driven flow, one additional scenario is performed without density and viscosity variations (sc 0.0), for comparison with the reference scenario. The thermal conductivity, specific heat and bulk density of the layers are not included in the sensitivity analysis series, but they were varied once to see what their qualitative effects are. The varied parameters are described below.

Table 2.2. Sensitivity analysis matrix for the T=40°C scenario series. Scenarios simulated are represented by a row. The reference scenario with according model input is shown in green. For each scenario (row), it is indicated what parameter is changed w.r.t. the reference scenario (orange) and by what factor (dfact). Also the residual input properties are listed.

	Scenario No.	Variation parameter	dfact	SEAWAT ON/OFF	Tinj °C	Qyearly m^3/yr	H_cap m	H_inj m	θ -	soil type	Kh m/d	Kv m/d	λ W/(m C)	$C_{p,s}$ J/(kg °C)	ρ_{bulk} kg/m^3	Well heat ON/OFF
	REF		1	ON	40	250000	30	30	0.3	sand	20	4	2.5	710	2148	OFF
									0.3	clay	0.05	0.01	2.5	1500	1800	
	0.0	SEAWAT	OFF	OFF	40	250000	30	30	0.3	sand	20	4	2.5	710	2148	OFF
									0.3	clay	0.05	0.01	2.5	1500	1800	
Hydrogeological	1.1	H_cap	0.5	ON	40	250000	15	15	0.3	sand	20	4	2.5	710	2148	OFF
									0.3	clay	0.05	0.01	2.5	1500	1800	
	1.2		0.67	ON	40	250000	20	20	0.3	sand	20	4	2.5	710	2148	OFF
									0.3	clay	0.05	0.01	2.5	1500	1800	
	1.3		1.5	ON	40	250000	45	45	0.3	sand	20	4	2.5	710	2148	OFF
									0.3	clay	0.05	0.01	2.5	1500	1800	
	1.4		2	ON	40	250000	60	60	0.3	sand	20	4	2.5	710	2148	OFF
									0.3	clay	0.05	0.01	2.5	1500	1800	
	2.1	H_inj	0.5	ON	40	250000	30	15	0.3	sand	20	4	2.5	710	2148	OFF
									0.3	clay	0.05	0.01	2.5	1500	1800	
	2.2		0.67	ON	40	250000	30	20	0.3	sand	20	4	2.5	710	2148	OFF
									0.3	clay	0.05	0.01	2.5	1500	1800	
	2.3		1.5	ON	40	250000	30	45	0.3	sand	20	4	2.5	710	2148	OFF
									0.3	clay	0.05	0.01	2.5	1500	1800	
	2.4		2	ON	40	250000	30	60	0.3	sand	20	4	2.5	710	2148	OFF
									0.3	clay	0.05	0.01	2.5	1500	1800	
	3.1	kv	0.5	ON	40	250000	30	30	0.3	sand	20	2	2.5	710	2148	OFF
									0.3	clay	0.05	0.01	2.5	1500	1800	
	3.2		2.5	ON	40	250000	30	30	0.3	sand	20	10	2.5	710	2148	OFF
									0.3	clay	0.05	0.01	2.5	1500	1800	
	3.3		5	ON	40	250000	30	30	0.3	sand	20	20	2.5	710	2148	OFF
									0.3	clay	0.05	0.01	2.5	1500	1800	
Operational	4.1	Qy	0.5	ON	40	125000	30	30	0.3	sand	20	4	2.5	710	2148	OFF
									0.3	clay	0.05	0.01	2.5	1500	1800	
	4.2		0.67	ON	40	166667	30	30	0.3	sand	20	4	2.5	710	2148	OFF
									0.3	clay	0.05	0.01	2.5	1500	1800	
	4.3		1.5	ON	40	375000	30	30	0.3	sand	20	4	2.5	710	2148	OFF
									0.3	clay	0.05	0.01	2.5	1500	1800	
	5.1	well casing	ON	ON	40	250000	30	30	0.3	sand	20	4	2.5	710	2148	ON
									0.3	clay	0.05	0.01	2.5	1500	1800	

2.3.2.1 *Operational parameters*

Injection temperature (T_{inj})

The main parameter to be changed is the injection temperature. Higher injection temperatures result in larger temperature and density gradients, giving higher heat fluxes and density driven flow losses respectively. Also, higher injection temperatures provide more energy to the subsurface system in an absolute sense and are therefore expected to affect the upper aquifer waters to a greater extent.

Yearly injected/extracted volume (Q_y)

The yearly injected volume (Qy) is the volume injected during the first half of the cycle, and extracted during the second half, using a sinusoidal pumping scheme. Increasing Qy increases thermal radius, the specific well discharge (m3/d per meter filter screen length) and average pore velocity. It determines the initial cylindrical thermal storage shape. For a given injection aquifer thickness (Hinj), larger injection volumes have lower A/V ratios and are associated with lower relative heat losses.

Heating from Well casing

Upon pumping, heat from the well casing can be conducted to layers penetrated by the borehole, adding heat to these layers. For each injection temperature, the well heat will be included in the model once to study its impact.

2.3.2.2 *Hydrogeological parameters*

Thickness of injection aquifer (H_{inj})

As wells are assumed to be fully penetrating, the thickness of the injection aquifer determines the filter screen length and the shape of the stored volume and hence has similar effect as Q_y. Larger injection aquifer thickness is associated with increased buoyancy tilting flow, according to Hellström.

Thickness of cap layer (H_{cap})

The thickness of the cap (clay) layer separating the two aquifers is varied. Changing this parameter directly changes the distance between the hot (top of injection aquifer) and cold (surface) temperature

boundary and thereby determines the thermal gradient in the soil profile overlying the injection aquifer. When H_{cap} is larger, the thermal impact on overlying layers is expected to decrease.

Vertical hydraulic conductivity (k_v)
Lower values of vertical hydraulic conductivity (kv) are expected to inhibit vertical flow hence density driven flow. By keeping the kH constant and changing the kV value, the sensitivity of efficiency to both the kH/kV ratio and kV was studied.

2.3.2.3 Soil properties not included in the Sensitivity Analysis

Thermal conductivity ratio ($\lambda_{sand}/\lambda_{clay}$)
Although thermal conductivities of clay and sand are equal in the sensitivity analysis, two scenarios were simulated in which sand has a higher thermal conductance, to study the qualitative effect of vertical heterogeneity.

Bulk soil density and heat capacity
High bulk soil densities and high heat capacities result in higher thermal retardation coefficients hence larger temperature travel times to overlying layers. The values used for these parameters are representative for several types of clay/sand formations. These parameters will not be considered in the sensitivity analysis, but a single simulation is performed to show their qualitative effects.

2.4 Assessment Framework

To address the research questions stated, specific results were assessed. The temperature distributions with time as well as the breakthrough times of the critical temperature (25°C) at the critical depth were expected to give most clarification on conditions favoring heat transport to upper layers. The thermal recovery efficiency after a certain amount of cycles of several modelled scenarios were compared as well, with specific attention to thermal storage shapes and buoyancy flow related parameters to find the effects of conduction and density driven flow on efficiency losses respectively.

2.4.1 Thermal impact on the surroundings

When temperatures in the upper aquifer exceed the critical temperature (T_{crit}) of 25°C, it is expected that the water quality of the aquifer is affected. This can have negative consequences when the aquifer is used for drinking water production or other purposes. Therefore it is critical to analyze to what extent this aquifer is thermally affected by the underlying injected volume of heat and how this relates to the hydrogeological and operational conditions. To obtain more insight in this, two types of results were evaluated: 1) the 1D steady state temperature distribution as calculated from the 1D steady state heat conduction theory and 2) the numerically simulated temperatures in space and time. The result of 1) is a vertical temperature distribution that the system theoretically moves towards on the long term, and is therefore important to find. It can be used for this purpose if successfully validated by the numerical model. 2) provides temperature distribution data in space and time. A set of temperature observation nodes registers the temperature changes at the critical depth D_{crit} (the bottom of the upper aquifer). The time needed for T_{crit} to break through at D_{crit} is called the breakthrough time. The breakthrough times were plotted versus the parameter variation factor to find the sensitivity of the breakthrough time to hydrological and operational parameters. Additionally, snapshots of 2D temperature distributions provide insight in the temperature development in time.

2.4.2 Thermal Recovery Efficiency of the system

The thermal recovery efficiency of a system after a certain amount of cycles was plotted versus the variation in hydrogeological and operational parameters with respect to the reference case to find what parameters primarily control efficiency. 2D axisymmetric temperature distribution visualizations can be used to observe heat distribution changes with time, so that density driven flow can be studied. The mixed convection ratio M and the characteristic tilting time t_0 are evaluated to see whether they properly predict buoyancy flow. Efficiency of all the scenarios of the sensitivity analysis is also plotted versus A/V and L/R_{th} ratio to see its relation to thermal storage shape.

2.5 Model

2.5.1 SEAWAT_V4 model

SEAWAT (Guo & Langevin, 2002) is a coupled version of the finite-difference code MODFLOW (Harbaugh et al. 2000) and MT3DMS (Zheng & Wang, 1999) programs, with a variable density flow (VDF) package. It is designed to simulate three-dimensional, variable-density saturated groundwater flow and multi-species transport. SEAWAT version 4 (SEAWATv4) (Langevin et al., 2007) is the more recent version of SEAWAT with added ability to simulate solute and heat transport simultaneously. Its viscosity package (VSC) also provides a set of functions to choose from, to describe fluid viscosity as a function of concentration and temperature, so that resistance to groundwater flow is described more accurately. Flexible equations for fluid density allow for a density description as a function of concentration, temperature and pressure.

Thanks to the similarity between the equations of solute and heat transport, the MT3DMS program that normally solves the solute transport can be used to model transport of heat, by treating it as a solute species. This requires manipulation of the solute species transport coefficients. Heat conduction is simulated by replacing the molecular diffusion coefficient by thermal diffusivity. Heat exchange between the solid and fluid is included in the simulation by using the mathematically equivalent process of solute sorption (Langevin et al., 2007). The governing equations used in SEAWATv4 do not describe chemical reactions like mineral precipitation and dissolution from temperature changes. SEAWATv4 is used to simulate several HT-ATES scenarios to obtain insight in the processes and parameters controlling heat transport in HT-ATES systems.

2.5.2 Mathematical formulations

2.5.2.1 Equations of state

An equation of state of a fluid defines the value of a property of a fluid, given its state parameters (like temperature, concentration, pressure). These relations are generally deduced from experiments in which state parameters were varied individually to see how the fluid property responded. For this study case, the response of both dynamic viscosity and density to changes in temperature, concentration and pressure are of interest.

Dynamic Viscosity

Dynamic viscosity [N m^{-2} s] is a property describing a fluid's resistance to flow. The dynamic viscosity of water is most sensitive to temperature, less sensitive to solute concentration and has a relatively weak dependence of pressure on the depth range considered here (Chaplin, 2017). Since in this study fresh water is simulated (near-zero solute concentration), the concentration is not important and the dynamic viscosity is only dependent of the temperature. Higher temperatures results in a lower dynamic viscosity. Several expressions for the relation of dynamic viscosity and temperature exists. The model in this study uses the definition of Voss & Provost (2010), where the dynamic viscosity [Pa s] depends on the temperature (in degrees Celsius) and the coefficients (A_1-A_4) that were provided to the model. The T in the denominator ensures that viscosity decreases with temperature.

$$\mu(T) = A_1 * A_2^{\frac{A_3}{T+A_4}} = 239.4 * 10^{-7} * 10^{\frac{248.37}{T+133.15}} \quad \text{(E2.26)}$$

Density

The equation of state for water density includes temperature, solute concentration and pressure: $\rho = \rho(T, C, P)$. The total differential equation is (Diersch & Kolditz, 2002):

$$d\rho = \left(\frac{1}{\rho}\frac{\partial\rho}{\partial T}\right)\rho dT + \left(\frac{1}{\rho}\frac{\partial\rho}{\partial C}\right)\rho dC + \left(\frac{1}{\rho}\frac{\partial\rho}{\partial P}\right)\rho dP \quad \text{(E2.27)}$$

The terms preceding the ρdT represent the volumetric thermal, solutal and pressure expansion coefficient, referred to as β_T, β_C, β_P respectively. β_P is also referred to as fluid compressibility. For a relatively small range in density these coefficients can be taken constant. Integration of the differential

equation then yields the following expression for the density with respect to the reference density at a reference temperature, concentration and pressure $\rho_0 = \rho(T_0, C_0, P_0)$:

$$\rho = \rho_0 \exp[\beta_T(T - T_0) + \beta_C(C - C_0) + \beta_P(P - P_0)] \quad \text{(E2.28)}$$

β_T is negative to make sure that higher temperatures than the reference temperature result in a lower density contribution. When the expression above is linearly approximated, the final expression for the equation of state for fluid density becomes:

$$\rho = \rho_0[1 + \beta_T(T - T_0) + \beta_C(C - C_0) + \beta_P(P - P_0)] \quad \text{(E2.29)}$$

Generally this form is used in describing the density in numerical modelling (Langevin et al., 2007). Looking at the structure of the equation, it becomes clear that the density of a fluid in a certain state is defined by taking a reference density taken at a reference state. This density is then corrected for temperature, solute concentration and pressure using a predefined volumetric expansion coefficient β. The volumetric pressure expansion coefficient β_P is negligible for confined aquifers at shallow depth, and this study does not comprise solute concentration, so that here the density is only controlled by the temperature of the water.

Impact of density and viscosity on flow

The relative importance of density and viscosity depends on the temperature range considered. For this study, the temperature range of 12-80°C applies (native groundwater temperature – maximal injection temperature). The viscosity is relatively more sensitive to temperature variations than density (see Figure 2.14, note scale). The dropped resistance to flow facilitates flow in all directions, favoring density driven flow as well. So in buoyancy flow, the flow is driven by the density differences, and viscosity determines the ease by which this occurs.

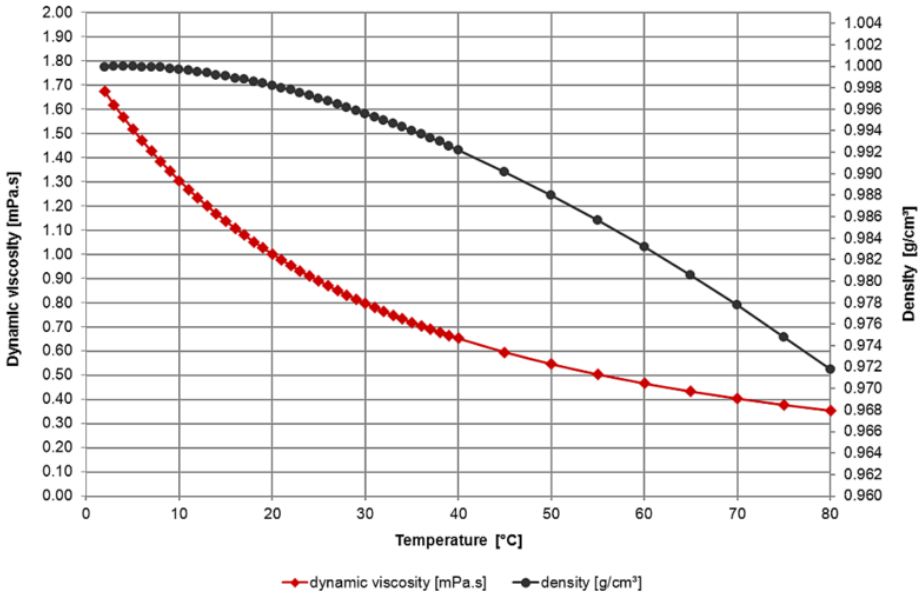

Figure 2.14. Dynamic viscosity (red) and density (black) dependence of temperature for pure water. After (Wagner & Kretzschmar, 2008)

2.5.2.2 Governing Equations

SEAWATv4 uses the governing equations for groundwater flow and solute transport as well as the equations of state for fluid density and viscosity as a function of state variables. The following governing equation from SEAWAT is used to describe the variable density flow (Guo & Langevin, 2002). Tensors and vectors are given in bold.

$$\nabla \cdot \left[\rho \frac{\mu_0}{\mu} \mathbf{K_0} \left(\nabla h_0 + \frac{\rho - \rho_0}{\rho_0} \nabla z\right)\right] = \rho S_{s,0} \frac{\delta h_0}{\delta t} + \theta \frac{\delta \rho}{\delta C} \frac{\delta C}{\delta t} - \rho_s q_s' \quad \text{(M1)}$$

with

ρ_0 the fluid density [M/L^3] at the reference concentration and temperature;
ρ the fluid density [M/L^3], calculated by the equation of state
μ the dynamic viscosity [ML^{-1}T^{-1}], calculated by the equation of state
μ_0 the dynamic viscosity [ML^{-1}T^{-1}] at the reference concentration and temperature
$\boldsymbol{K_0}$ the hydraulic conductivity tensor of a solid material saturated with the reference fluid [LT^{-1}];
h_0 the hydraulic head [L] in terms of the reference fluid properties
$S_{s,0}$ the specific storage [L^{-1}]
t the time [T]
θ the porosity [-]
C the salt concentration [ML^{-3}] and
q_s' a source or sink [T^{-1}] of fluid with density ρ_s

A general form of the solute transport equation solved in the MT3DMS package is:

$$\left(1 + \frac{\rho_b K_d^k}{\theta}\right) \frac{\delta(\theta C^k)}{\delta t} = \nabla \cdot \left[\theta \left(\boldsymbol{D_m^k} + \boldsymbol{\alpha} \frac{\boldsymbol{q}}{\theta}\right) \cdot \nabla C^k\right] - \nabla \cdot \left(\boldsymbol{q} C^k\right) - q_s' C_s^k \quad \text{(M2)}$$

where $D_m^k + \boldsymbol{\alpha} \frac{\boldsymbol{q}}{\theta} = \boldsymbol{D}$

ρ_b the bulk density [ML^{-3}] of the soil
K_d^k the distribution coefficient of species k [L^{3}M^{-1}]
C^k the concentration of species k [ML^{-3}]
D_m^k the molecular diffusion coefficient for species k [L^{2}T^{-1}]
$\boldsymbol{\alpha}$ the dispersivity tensor [L]
$\mathbf{q}$ the specific discharge [LT^{-1}],
$\boldsymbol{D}$ the hydrodynamic dispersion coefficient tensor [L^{2}T^{-1}], which is the sum of a molecular diffusion term and a dispersion term
C_s^k the source or sink concentration [ML^{-3}] of species k

Thorne et al. (2006) manipulated the heat transport equation to show its similarity with the solute transport equation, resulting in the following thermal transport equation form: (Thorne et al., 2006):

$$\left(1 + \frac{1-\theta}{\theta} \frac{\rho_s}{\rho} \frac{c_{p,s}}{c_{p,f}}\right) \frac{\delta(\theta T)}{\delta t} = \nabla \cdot \left[\theta \left(\frac{\lambda_b}{\theta \rho c_{p,f}} + \boldsymbol{\alpha} \frac{\boldsymbol{q}}{\theta}\right) \cdot \nabla T\right] - \nabla \cdot (\boldsymbol{q} T) - q_s' T_s \quad \text{(M3)}$$

With $\rho_b = \rho_s(1-\theta)$ and $\frac{\lambda_b}{\theta \rho c_{p,f}} = D_{m\_temp}$

ρ_s the density [ML^{-3}] of the solid
$c_{p,s}$ the specific heat capacity of the solid [L^2 T^{-2}K^{-1}]
$c_{p,f}$ the specific heat capacity of the fluid [L^2 T^{-2}K^{-1}]
λ_b the bulk thermal conductivity of the aquifer material [ML^{3}T^{-2}K^{-1}]
T_s the source temperature [K]

In M2 and M3, the advection (or convection) and dispersion are described in the same way for solute or heat transport. The adaptions applied to M2 to obtain M3 are needed to correctly include the processes heat conduction and thermal equilibration of the solid and fluid phase. These adaptions are explained below.

2.5.2.3 *Thermal diffusivity and Thermal Distribution Coefficient*

Molecular diffusion for solutes (Fick's law) and heat conduction (Fourier's law) are mathematically similar and only the molecular diffusion coefficient term (D_m^k, see M2) needs to be replaced by the bulk thermal diffusivity ($D_{m,temp}$, M3) in order to calculate heat conduction with the MT3DMS program. $D_{m,temp}$ is calculated as follows:

$$D_{m\_temp} = \frac{\lambda_b}{\theta \rho c_{p,f}} \quad \text{(M4)}$$

The bulk thermal conductivity (λ_b) is derived from the fluid and solid thermal conductivities and porosity, according to the definition of Hughes & Sanford (2004):

$$\lambda_b = \theta \lambda_{fluid} + (1 - \theta)\lambda_{solid} \quad \text{(M5)}$$

Only isotropic thermal conductivities can be entered in the model.

In M2, solute sorption is included in the factor preceding the time derivative on the left hand side of the equation. A similar term is used in M3, representing the temperature equilibration between the fluid and solid. These terms are referred to as retardation coefficients and cause a solute or temperature front to move slower than the average linear flow velocity because of sorption or thermal retardation respectively. For thermal equilibration, the distribution coefficient of a solute species (K_d^k [m^3/kg]) must be replaced by the thermal distribution factor $K_{d,temp}$, defined by the ratio of specific heat of solid and fluid, and the fluid density:

$$K_{d,temp} = \frac{c_{p,s}}{\rho c_{p,f}} \quad \text{(M6)}$$

A linear sorption isotherm is used for the thermal equilibration, meaning that the thermal energy distribution between the fluid and the solid phase in a cell is always in equilibrium. This also implies that the process of thermal equilibration between fluid and solid occurs instantaneously.

A limitation for heat conduction and thermal equilibration simulation is that in M4 and M6, the fluid density ρ is fixed at 1000 kg/m^3 and thus $D_{m,temp}$ and $K_{d,temp}$ will not react to temperature induced density variations in the fluid. However, for the temperature range used in this research, the variation in $D_{m,temp}$ and $K_{d,temp}$ is relatively low and can therefore be neglected. Specific heat, thermal conductivity and dispersivity are all constant in time, but may differ per model layer.

2.5.3 Modelling axisymmetric flow

Three-dimensional models usually have high computational costs. In MODFLOW, flow and transport for a cylindrical soil profile can be simulated by a two-dimensional axisymmetric model that is much faster, but axisymmetric groundwater flow from or to a vertical well is then required. In the literature, several methods exist for the conversion of a 3D model domain to an axisymmetric 2D domain (Langevin, 2008),(Wallis et al., 2013) (Louwyck et al., 2014). The method of Langevin is used here. This method is proven to be successful in accurately simulating coupled variable-density ground water flow and solute transport in radially homo- and heterogeneous multi-aquifer systems.

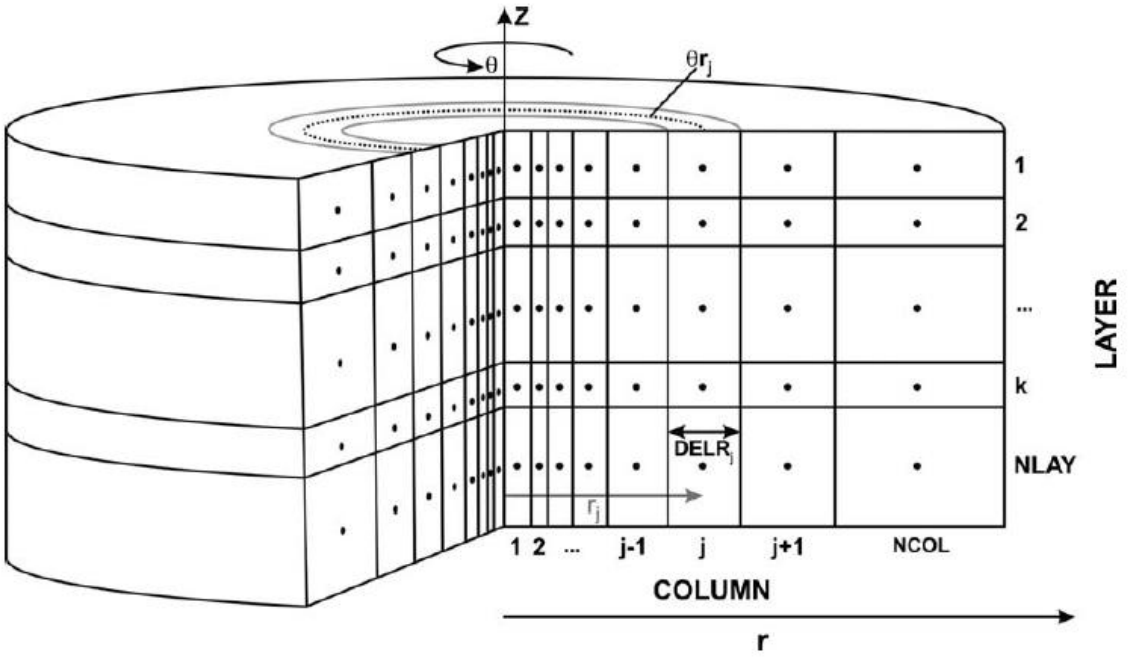

Figure 2.15. Schematic view of an axially symmetric profile model. (Langevin, 2008)*, after* (Reilly & Harbaugh, 1993)

Langevin takes a wedge out of the axisymmetric flow domain and translates this into terms of MODFLOW, see figure 2.15. The wedge then represents (a part of) a concentric ring through which flow occurs. To successfully incorporate the increasing flow area and storage volume of the wedge with radius in the axisymmetric model, the transmissive and storage properties of the model have to be adjusted manually. That means that for this study, porosity, horizontal and vertical hydraulic conductivity, specific storage and bulk density need to be scaled to the radius r_j at the middle of the cell, according to the following conversion:

$$P_j = \theta r_j P \qquad \text{(M7)}$$

With P_j the adjusted parameter value for cell j, r_j the radial distance to the center of cell j, θ the angle of the wedge open to flow and P the original parameter value. This research applies an angle of 2π to represent a cylindrical modelled domain. This allows for a proper study of the thermal energy storage in a cylindrical soil profile.

The thermal distribution factor $K_{d,temp}$ needs no individual scaling, since the retardation is already adjusted by the scaling factor applied to the bulk density (see M3). Heat conduction occurs through a certain area and since area of the cell rings increase with radius, the thermal diffusivity ($D_{m,temp}$) of a material needs to increase as well. The scaling factor is already applied to the porosity preceding $D_{m,temp}$ in M3, so that also for the thermal diffusivity no further scaling is needed.

2.5.4 Model Setup

2.5.4.1 Programs

SEAWATv4 is used to model three-dimensional, saturated variable-density groundwater flow with the MODFLOW and MT3DMS programs. Its capacity to treat heat as a solute species is exploited to simulate various heat transport scenarios. An axisymmetric model is used to model a 3D axially symmetric soil profile with a 2D MODFLOW model domain hence with relatively limited computational costs. Programming language Python (van Rossum, 1995) provides a package FloPy (M. Bakker et al., 2016) that is used to set the input parameters and run the SEAWATv4 code. The output was extracted, visualized and the results were interpret.

2.5.4.2 Assumptions

The models hydrological properties are laterally homogeneous and vertically heterogeneous, meaning that a multi-layered system was modelled. The axisymmetric modelling does not allow regional hydraulic gradients to be present, so all hydraulic heads are a result of the pumping activity of the well. Conclusions drawn from the scenarios simulated can thus be applied to systems where no or only little regional groundwater flow is present.

2.5.4.3 Spatial discretization

The model has 50 columns. The widths of the first (0.5m) and the last (500m) columns are specified and the column widths in between increase linearly on a log scale. This results in an increasingly finer horizontal grid resolution towards the well and a total horizontal extent of the model of 3800m. With this modelled domain, simulation results were not affected by the boundary conditions. The vertical grid resolution is 1m so that the number of model layers is equal to the thickness (in m) of the soil profile modelled. The model has 1 row.

For the scenarios where the well heat radiation is considered, two additional columns of width 0.05m and 0.20m are added directly to the right of the first column, representing the PVC well screen and bentonite gravel pack respectively, see fig 2.16. These columns will have IBOUND=1 i.e. open to flow to allow for heat transport simulations. Thermal conductivity values can be applied according to the properties of the well screen and gravel pack. For each timestep, a constant temperature was applied to the well screen, depending on the water temperature flowing through the well. Upon injection, this temperature is equal to the injection temperature minus 5°C. During production, the temperature is equal to the average temperature of the produced water. In this way, thermal transport from the well screen through the bentonite gravel pack to the aquifer could be studied.

2.5.4.4 Time discretization

A cycle length of 360 days with timesteps of 30 days was used. This ensures that 1) an equal amount of timesteps is dedicated to injection and production and 2) the time discretization and computational costs of the model are balanced. Courant numbers <1 were found for the area of interest i.e. around the thermal radius. Conveniently, one cycle comprises 12 timesteps, which can be thought of as months. Note that in practice the injection/production discharge is constant during 1 timestep, so that the sinusoidal pumping scheme is stepped because of the 12 timesteps with different discharges in time.

2.5.4.5 Boundary and initial conditions

A schematic view on the model domain is presented in figure 2.16. Constant hydraulic head boundaries are applied to the top layer and to the outer column of the model. The change in flow pattern resulting from the well activity is not influenced by the boundaries of the domain. Constant temperature boundaries of 12°C apply to the top (surface) and outer column of the model. This results from the assumption that the average groundwater temperature is determined by the average yearly surface temperature, which is taken 12°C in this research. Initial heads and temperatures are 0m and 12°C respectively, for the complete model domain. The clay layer at the bottom of the model needs to be thick to ensure that hydraulic heads and temperatures in the injection aquifer are not influenced by the lower boundary of the model.

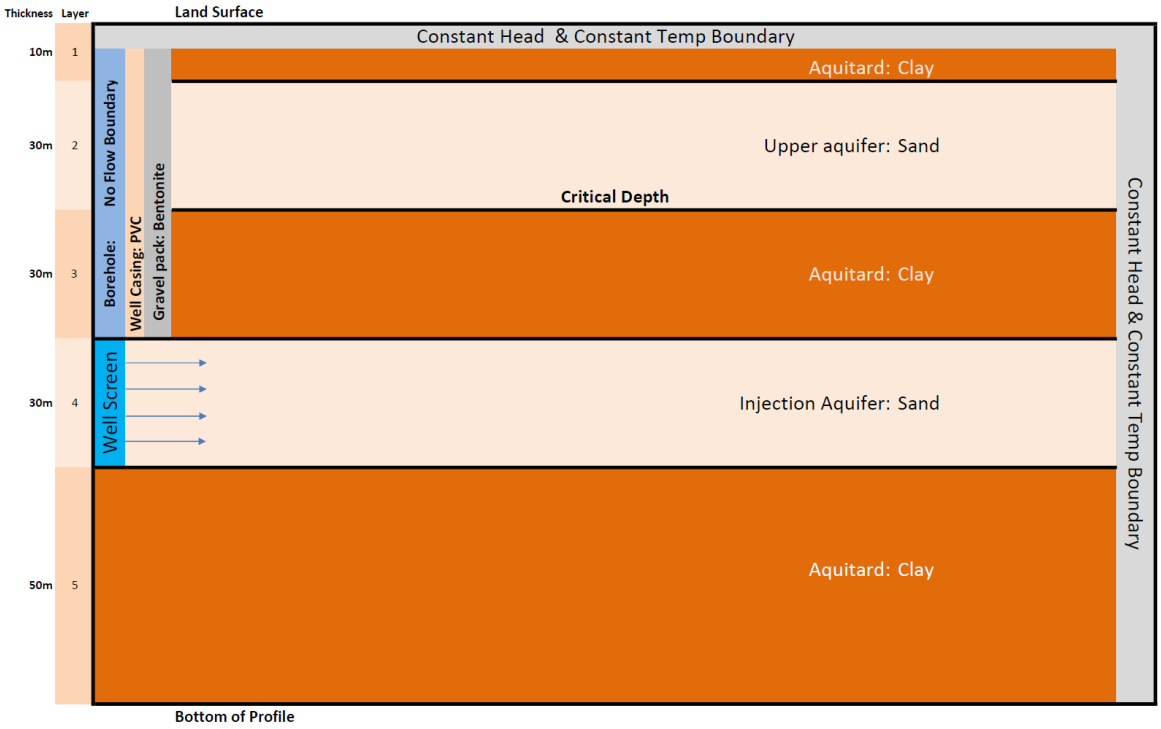

Figure 2.16. Schematic of the model domain (not to scale), showing the horizontal sand and clay layers with thickness and the constant temperature and hydraulic head boundaries. The first column comprises the well screen (water injection cells) in the injection aquifer and the borehole above it, with IBOUND=0. The critical depth is the bottom of the upper aquifer. Observation nodes were located at this depth, at different distances from the well. Well Casing and Gravel pack cell columns are only applied for the scenarios simulating heat conduction from the borehole. Arrows are added to indicate water flow upon injection.

2.5.4.6 Water properties

The density and dynamic viscosity of water are only dependent of the temperature and calculated from the equations of state. The reference temperature and density used are 25°C and 1000kg/m^3 respectively. The thermal expansion coefficient is -0.35, representing the slope of the linear equation of state for water density. This results in a density-temperature relation that is most accurate around 40°C. At lower water temperatures than 40°C, the simulated water density is slightly overestimated hence the density difference with a 40°C water body is overestimated as well. For water temperatures higher than 40°C, the density is moderately overestimated in the model, giving similar effects. However, for the simulated temperature range, the difference between linearized (modelled) and real density of water is limited to <10kg/m^3 hence <1% of the reference density, the effects on the accuracy of the model is expected to be small. The reference density, reference temperature and slope of the equation of state for density are all provided to the model. Water has a thermal conductivity of 0.58 W/m/K and a specific heat of 4183 J/kg/K.

2.5.4.7 Hydrogeological and thermal properties

The soil properties assigned to the model domain were shown in table 2.1 for the reference scenario and in table 2.2 for all other scenarios of the sensitivity analysis. The hydraulic conductivity for the clay formations is very low so that the injection aquifer is practically confined. The longitudinal and transversal dispersivity is 0.1 and 0.01m for all cells respectively, for all scenarios. Thermal properties of the reference scenario are listed in table 2.3. The values presented are based on the literature (Hamdhan & Clarke, 2010; British Geological Survey, 2011; Abu-Hamdeh, 2003) and use a water density of 1000kg/m^3.

Table 2.3 Thermal soil properties used for the model, based on literature. Properties needed as model input are underlined. Thermal conductivity of the solid relates to bulk thermal conductivity by the porosity (Hughes and Sanford, 2004). Bulk specific heat is related to the specific heat of the solid phase by porosity and specific heat of water.

Property	Symbol	Unit	Value	
			Sand	Clay
Thermal conductivity of solid	λ_s	J/(m °C)	3.323	3.323
Bulk thermal conductivity	λ_b	J/(m °C)	2.5	2.5
Thermal diffusivity	$D_{m,temp}$	m^2/d	0.1721	0.1721
Specific heat of solid	$C_{p,s}$	J/(kg °C)	710	1500
Bulk specific heat	$C_{p,b}$	J/(kg °C)	1752	2305
Thermal distribution coefficient	$K_{d,temp}$	m^3/kg	1.697E-4	3.586E-4

2.5.4.8 Specific SEAWAT model information

The PCG package is used to simulate groundwater flow and the standard finite-difference method with upstream weighting is used for the advection package, with a Courant number of 1. Vandenbohede et al. (2014) showed that for successfully simulating axisymmetric heat transport in SEAWAT, the convergence criterion for heat transport must be set to a much smaller value, from the usual 10^{-6} used for a solute species to 10^{-10} for a temperature species (Vandenbohede et al., 2014). This is because heat conduction occurs similarly to solute diffusion but at a higher rate. Grid discretization needs to be finer towards the well and the filter screen should be subdivided into more cells to accurately model heat conduction after injection. This was all incorporated in the model.

2.5.4.9 Validation

Several studies have shown that 3D axisymmetric flow around a vertical well can be successfully modelled using a 2D axisymmetric model (van Lopik, 2015)(Wallis et al., 2013)(Langevin, 2008). This was proven by benchmark tests and by numerical model validation using field data of the Auburn University (Tsang et al., 1981).

The model is assumed to be laterally homogeneous. Lateral heterogeneities in hydraulic conductivity can result in preferential flow paths, resulting in dispersed temperature fronts. However, the effect of increasing heterogeneity in hydraulic conductivity is similar to increasing dispersivity. This is natural because heterogeneity in soils is the cause for dispersion effects, and the inclusion of dispersion in the general transport equation is a way to account for pore scale heterogeneity in a macro scale model. Since the dispersion is proven not to be of great importance for the thermal front at larger distance from the well, heterogeneity in hydraulic conductivity is not expected to significantly alter the model results either.

In order to perform long-term simulations, the timestep used is 30 days. Courant numbers exceed 1 close to the well, but further away from the well where flow velocity is smaller and grid size is larger the Courant conditions are satisfied and advective transport can be modelled appropriately. Smaller timesteps may result in differences in absolute values of the output. However, the sensitivity analysis results aim to explain the relative differences between the scenarios and it is not expected that varying timesteps gives considerably different trends. However, it is advisable to use the same timestep for all scenarios performed in the sensitivity analysis for a reliable comparison between scenarios.

Heat conduction and thermal retardation are described in the dispersion and reaction package of SEAWATv4 respectively. The thermal diffusivity and distribution coefficients (which are independent

of temperature) can be successfully used by manipulating the diffusion coefficient and the retardation coefficient respectively, as was proven in earlier studies (see top of this section). Definitions for bulk thermal conductivity and for dynamic viscosity as a function of temperature are provided according to the theory of Hughes and Sanford (2004) and Voss (1984) respectively. Other relations can be applied as well, giving slightly different values and results.

This research performs a sensitivity analysis; it aims to obtain insight in the relative change of the output, upon variation of one parameter. This means it is more important how the system changes upon parameter variation, than how accurate the produced model output value is.

3 Results

3.1 Thermal recovery efficiency

3.1.1 Sensitivity Analysis

The 50th-cycle efficiencies of all the scenarios are shown in Table 3.1. Green and red colors represent high and low efficiencies respectively. The varied parameters ('Variation parameter') and the variation factor with respect to the reference scenario ('dfact') are shown for each scenario (each row), for the four different injection temperatures (T=20, T=40, T=60, T=80°C). For all scenarios (rows), the efficiencies decrease with increasing injection temperature (T_{inj}) except for the cases where no density and viscosity differences are included (SEAWAT=OFF, sc0.0): here, the efficiencies are independent of injection temperature, in agreement with the theory of Kranz & Bartels (2009). The efficiency is practically insensitive to the cap layer thickness ('H_{cap}', sc 1.1-1.4) and to heating from the well casing ('well casing' sc 5.1). The lowest efficiencies were obtained for scenarios with high injection temperature in combination with either large injection aquifer thickness or small yearly injection volume. The sensitivities to injection aquifer thickness (H_{inj}, sc2.1-2.4), vertical hydraulic conductivity (k_V, sc 3.1-3.3) and yearly injected volume (Q_y, sc 4.1-4.3) are graphically presented in figure 3.1, showing the efficiency relation to the variation factor (dfact). Note that the lines are added to show the alignment and may not be suitable for extrapolation.

Tabel 3-1 For each scenario (row), the varied parameter and the variation factor ('dfact') with respect to the reference scenario is shown, as well as the according efficiency, for each injection temperature.

	Scenario No.	Variation parameter	dfact	Injection Temperature efficiencies T=20	T=40	T=60	T=80
	REF		1	82.412	81.507	79.195	75.711
	0.0	SEAWAT	OFF	82.47741	82.47741	82.47741	82.47741
Hydrogeological	1.1	H_cap	0.5	82.449	81.455	78.912	75.158
	1.2		0.67	82.445	81.505	79.078	75.451
	1.3		1.5	82.371	81.474	79.193	75.784
	1.4		2	82.445	81.460	79.189	75.804
	2.1	H_inj	0.5	78.301	78.245	78.019	77.498
	2.2		0.67	80.269	80.061	79.395	78.078
	2.3		1.5	83.846	81.058	75.731	69.253
	2.4		2	84.438	79.680	72.054	63.520
	3.1	kv	0.5	82.429	81.734	79.820	76.707
	3.2		2.5	82.395	81.286	78.659	74.962
	3.3		5	82.386	81.181	78.427	74.677
Operational	4.1	Qy	0.5	81.249	79.208	74.852	69.216
	4.2		0.67	81.799	80.309	76.881	72.177
	4.3		1.5	82.861	82.347	80.891	78.462
	5.1	well casing	ON	82.201	81.323	79.046	75.594

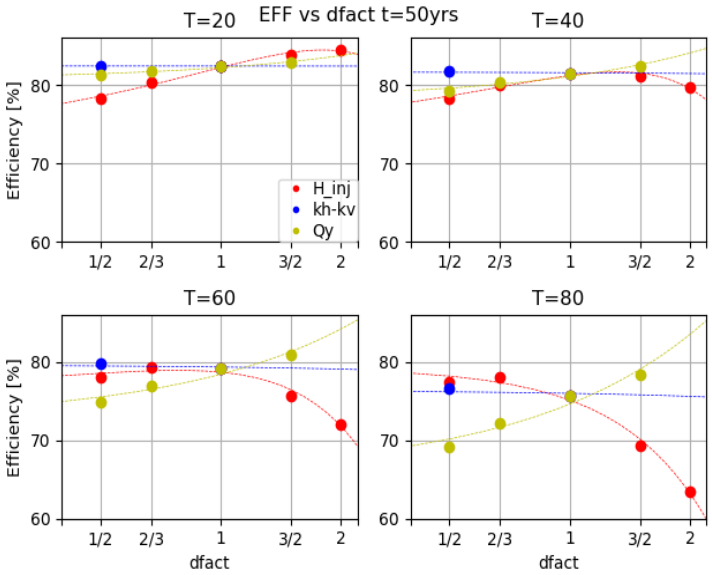

Figure 3.1 The efficiency sensitivity to H_{inj}, Q_y and k_V, graphical representation of table 3.1. dfact = 1 represents the reference scenario. Steeper trends indicate a higher sensitivity.

For a given injection temperature, the efficiency is nearly insensitive to the vertical hydraulic conductivity. Efficiency increases nearly linearly with increasing yearly injected volumes and the sensitivity is higher for higher injection temperatures. For the T=20°C scenarios simulated, efficiency increases with increasing injection aquifer thickness because the thermal shape moves towards the optimal A/V ratio for the given injected volume. The opposite happens for the higher injection temperature scenarios: efficiency considerably decreases when the injection aquifer thicknesses increase with respect to the reference scenario (dfact>1). Decreasing the injection aquifer thickness w.r.t. the reference scenario (dfact ≤ 1) has only moderate effect on efficiency. For scenarios with injection temperatures 60 or 80°C, the tipping point (or kink) in the course of the relation between efficiency and injection aquifer thickness is located close to the reference scenario value (dfact=1, H_{inj}=30m). Note that these observations apply to the scenario range modelled, which is based on the chosen reference scenario.

Additional scenarios were performed to find the sensitivity of efficiency to 1) the specific heat of the solid clay phase, 2) the bulk density of the cap clay layer and 3) the thermal conductivity of sand. Increasing either of these parameters by 20% w.r.t. their reference scenario value had no significant impact on the efficiency.

3.1.2 Heat losses by conduction and density driven flow

The 10th cycle efficiencies of the scenarios with injection temperatures of 20°C were added to the results of earlier studies of Bloemendal & Hartog (2018), who also used the 10th cycle efficiency, Doughty (1982) and van Lopik (2015). Figure 3.2 shows the same linear relationship between A/V ratio and efficiency. Differences between the scenarios are likely to be caused by different dispersion coefficients, cycle lengths and model setups.

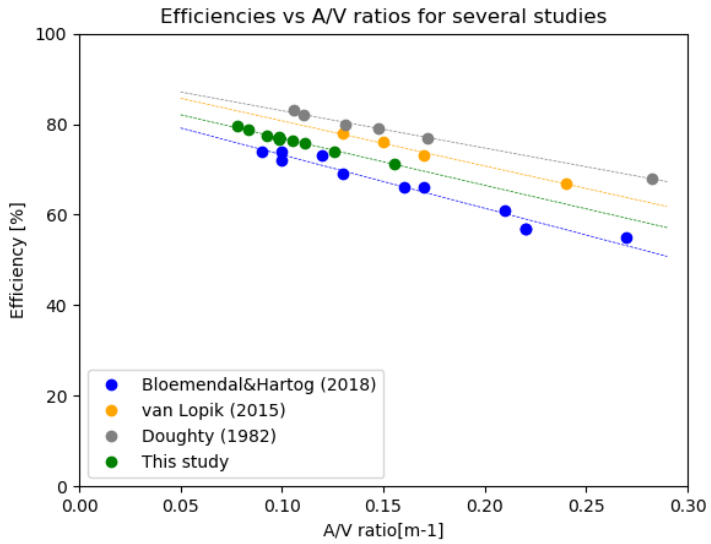

Figure 3.2 efficiencies vs A/V ratios for scenarios where no density driven flow and regional groundwater movement is included. The data from this study are the 10th cycle efficiencies of the T=20°C scenarios.

The 50th-cycle efficiencies of all the simulated scenarios were plotted in figure 3.3a versus the A/V ratio of the injected cylindrical thermal storage volume. The pattern is independent of the cycle number at which efficiency was taken. For higher injection temperatures (T≥40°C) the efficiencies are not linearly related to A/V anymore. Indicative trendlines are added for all temperature scenarios of the yearly injected volume (blue) and for the T=60 and T=80°C scenarios of the injection aquifer thickness (red).

- The efficiency is linearly related to A/V for scenarios where the yearly injected volume is changed (sc4.1-4.3), and the sensitivity to A/V is higher for higher injection temperatures.
- The efficiencies of the injection aquifer thickness scenarios (sc2.1-2.4) are non-linearly related to A/V.
- The other scenarios (well casing, H_{cap}, k_V) have equal A/V ratio as the reference scenario but only slightly different efficiencies and are therefore not labeled in figure 3.3a.

Figure 3.3a and fig 3.1 both show that for high injection temperatures, there is a critical injection aquifer thickness. When this critical thickness is exceeded, efficiency decreases strongly. This critical thickness is smaller for higher injection temperatures.

Buoyancy flow changes the storage shape from cylindrical to conical so that the A/V ratio and the conduction losses are increased. Hellstrom suggested that buoyancy flow is considerable when t_0<cycle length. The characteristic tilting times (t_0) of the reference scenarios at 20, 40, 60 and 80°C are calculated with the theory of Hellstrom (E2.22). They are 1298, 197, 106 and 75 days respectively. For this research then (cycle lengths of 360 days), buoyancy flow should become important for T ≥ 40°C. Figure 3.3b is the same plot as fig 3.3a, but the A/V ratios were adjusted for scenarios where t_0<360 days. The new (higher) A/V ratio is calculated by assuming a conical thermal storage shape with a 60° angle of the interface with respect to the vertical. Since there is still no good alignment of the points at higher temperatures now that shape changes are included, the energy losses are not only caused by extra conduction losses because of the shape change. This means that density driven flow adds to energy losses when injection temperatures are higher than 20°C, and especially when injection aquifer thickness is high or yearly injection volume is low.

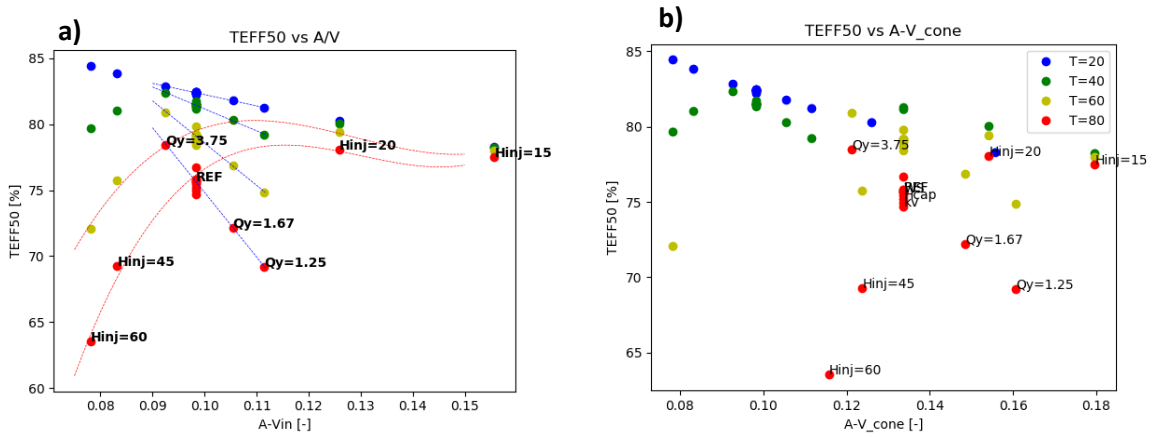

Figure 3.3 Efficiencies versus A/V ratio of the cylindrical (a) and the conical (b) thermal storage volumes. Labels indicate the parameter varied with respect to the reference scenario. Colors indicate injection temperature. for a), lines are added to show the relation of A/V of H_{inj} and Q_y scenarios with Efficiency

Efficiencies of the scenarios were plotted versus the L/R_{th} value (figure 3.4) showing that for low injection temperatures, the general trend is that higher L/R_{th} ratios result in higher efficiencies, but the opposite is true when injection temperatures increase. Scenarios with low L/R_{th} values (L/R_{th}<0.4) show small (<5% efficiency) differences in efficiency between T=20°C and T=80°C scenarios, but for 0.5<L/R_{th}<1.4, this difference increases to ~20%. The optimal L/R_{th} value for scenarios without density driven flow and regional groundwater flow is 1.5-2 (Doughty, 1982), but the optimal values for the T=40, 60 and 80°C scenarios are all around 0.4 for the scenarios simulated. So the optimal L/R_{th} decreases for higher injection temperatures, meaning that 'pancake' storage shapes (L/R_{th}<0.5) are more favorable for efficiency at higher injection temperatures, when density driven flow can occur.

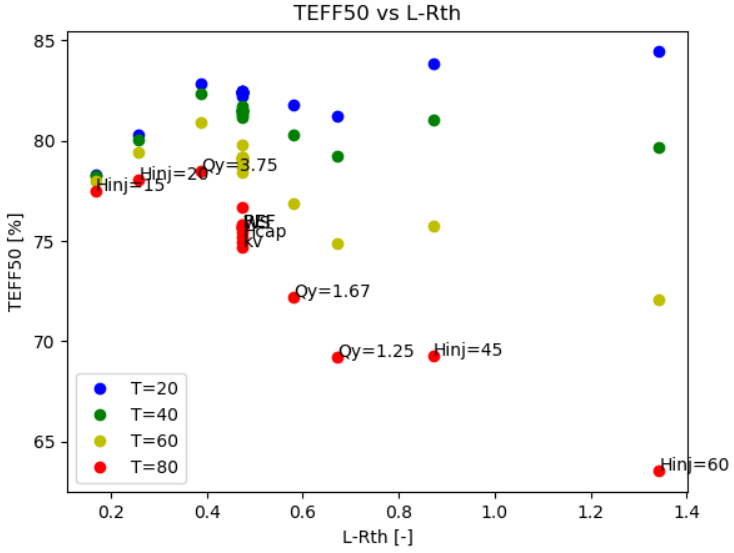

Figure 3.4. 50th cycle efficiencies vs. L/R_{th} of the cylindrical injected volume. L is filter screen length (m) and R_{th} is thermal radius. Colors indicate injection temperatures. Labels show what parameter is varied w.r.t. the reference parameter.

The sensitivity analysis results and figures 3.1, 3.3 and 3.4 showed that higher injection aquifer thickness and low injection volume result in low efficiencies. The combination of these two most dominant parameters is plotted versus the efficiency in figure 3.5, showing that for higher temperature scenarios, an optimum Q_y/H_{inj} ratio exists. This optimum decreases and shifts to higher values when injection temperatures increase. Some spread exists in efficiency for equal Q/H_{inj} values. The labels show that for the same Q_y/H_{inj} value (~4200m^2/yr), increasing H_{inj} results in lower efficiency than decreasing Q_y. The lines are representative for a conventional range of yearly injection volumes

(1.00 – 3.75 x10^5 m^3/yr). Efficiencies become increasingly lower when Q_y/H_{inj} drop lower than 10,000 m^2/yr. This may be a minimal critical value of Q_y/H_{inj} to consider in the design of HT-ATES systems. Note again that this applies to the scenario range simulated.

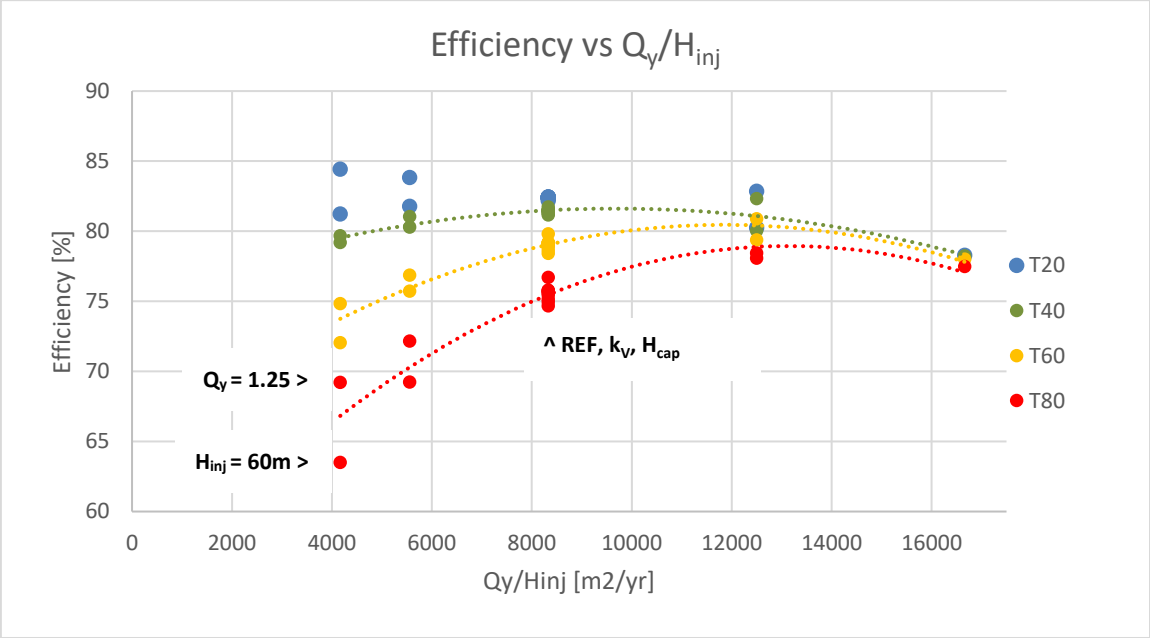

Figure 3.5. The efficiencies of all scenarios plotted vs their Q_y/H_{inj}. Dotted lines indicate the trends for the different injection temperatures. Labels (Q_y =1.25 x 10^5 m^3/yr, H_{inj} =60m) show that for two scenarios with equal Q_y/H_{inj}, increasing the H_{inj} gave lower efficiency than decreasing Q_y.

Figure 3.6 a-d shows how density driven flow affects the thermal recovery efficiency in two scenarios with injection temperature of 80°C. Isotherms are indicated in black and yellow. The figure shows the temperature distribution at the end of the 49th cycle (left hand side) and halfway the 50th cycle (right hand side), for a scenario with injection aquifer thicknesses of 15m (upper figures) and 60m (lower figures). The 50th cycle efficiencies for the small and large injection aquifer thickness scenarios are 77% and 64% respectively. The following was observed:

- More buoyancy flow occurred for the large injection aquifer thickness scenario, resulting in a larger volume of cold water produced at the bottom of the filter screen and more residual hot water at the top of the injection aquifer after the production period(fig 3.6c).
- Even though the A/V ratio of the initially cylindrical thermal storage volume is relatively high for small injection aquifer thickness (fig 3.6 a-b), the fact that only little buoyancy flow is allowed ensures that the bulk of the hot water is recovered after the production period and efficiency remains satisfactory.
- The thermal radius of the cylindrical volume is smaller for the H_{inj}=60m scenario (fig 3.6d), so that upon rotation of the interface, cold water arrives earlier at the bottom of the filter screen, giving lower efficiency.
- Despite the thermal radius of the 15m scenario is larger, the radial extent of the thermal impact on upper layers is larger for the 60m scenario because more residual warm water is left at the top of the injection aquifer after extraction (fig3.6c-d)
- For the 15m scenario, thermal effects on deeper formations are considerably larger (fig 3.6a-b).

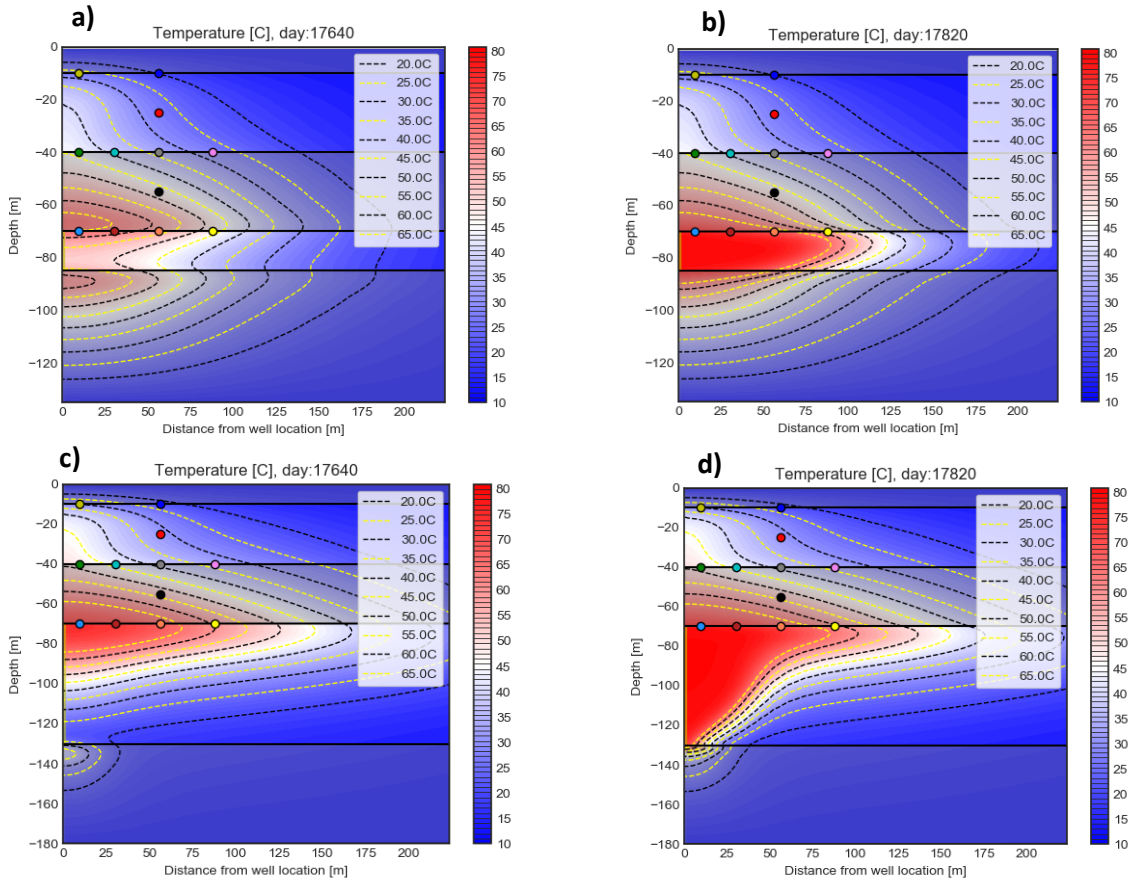

Figure 3.6. 2D visualizations of the axisymmetric temperature distributions for the scenario with injection aquifer thickness of 15m (top figures) and 60m (bottom figures). Left figures show the temperature distributions at the end of the 49th cycle, right hand side figures show temperature distributions after the injection period of the 50th cycle. Isotherms in yellow and black.

Additional model runs produced 2D temperature distribution snapshots like figure 3.6, but with a higher temporal resolution. They showed that buoyancy flow was most considerable towards the end of the injection period, when the interface was located farther from the well (figures not shown). The mixed convection ratio (M) of Ward et al. is highest at this point in time and space (interface far from well), meaning that buoyancy flow becomes important relative to the forced convection. In Figure 3.7a and b, the efficiencies are plotted versus M (E2.20) using the horizontal and vertical hydraulic conductivity for the calculation of the free convection respectively. In figure 3.7a M is approximately quadratically related to the efficiency, although the relation is merely a zone than a sharp line. Note that because of the definition of the dimensionless density difference (E2.22), M is negative. Buoyancy flow was expected when M < -0.1. According to Ward et al. then, all scenarios of T≥40°C predicted buoyancy flow. The model results however show that the efficiency range of scenarios with injection temperature of 40°C is not considerably lower than for 20°C. A significant decrease in efficiencies of the simulated scenarios occurs only for M< -2. Figure 3.7b shows that even though a low M was calculated for scenarios with high vertical hydraulic conductivity, efficiencies were not considerably lower. This shows that the role of vertical hydraulic conductivity in density driven flow losses is overestimated by M. The fact that M is defined based on the maximal thermal radius (i.e. at the end of the injection period) and that it is related to efficiency hints that heat losses are importantly determined by buoyancy flow occurring at the end of the injection period. This matches the observations done.

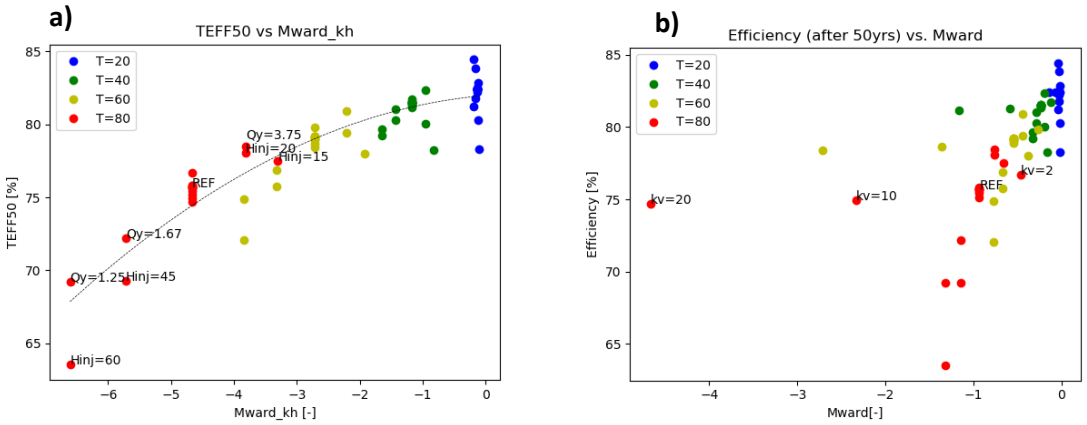

Figure 3.7. Efficiencies versus mixed convection ratio (M) as calculated by Ward et al. a) M calculated using the horizontal hydraulic conductivity of the scenario, b) right: M calculated using the vertical hydraulic conductivity of the scenario. Labels indicate the T=80°C scenarios

3.2 Thermal impact on overlying layers

3.2.1 Analytical 1D steady state heat conduction model

An analytical model was constructed to find the 1D steady state vertical temperature distribution, given the top/bottom constant temperature boundaries, and the thicknesses and thermal conductivities of the layers overlying a HT-ATES injection aquifer. This represents the temperature distribution the system moves to on the long term. Using the injection temperatures as the hot boundary condition, the vertical 1D steady state temperature distributions of the reference scenarios with injection temperatures of 20, 40, 60 and 80°C were calculated and are shown in figure 3.8a. Variety in the thermal conductivity of different soil layers result in a kink in the steady state temperature distribution (figure 3.8b). The interplay between the thickness of a layer and its thermal conductivity determines the deviation of the kinked profile relative to the linear temperature distribution (see E2.10). A lower thermal conductivity of the separating clay layer compared to the sand layer decreases the steady state temperature at the critical depth (-40m in figure 3.8). For the reference scenarios, the relative decrease in the steady state temperature at the critical depth by going from equal (λ_{clay}= λ_{sand}=2.5W/m/K) to different (λ_{clay}=2.5, λ_{sand}=3.0 W/m/K) thermal conductivity is 3.6%, 7.1%, 8.6% and 9.6% for injection temperatures of 20, 40, 60 and 80°C respectively (figure 3.8b). So given the clay-sand-clay lithology of the layers overlying the injection aquifer in the reference scenario, the effect of different thermal conductivity in clay and sand layers (with λ_{sand}> λ_{clay}) on the steady state temperature at the critical depth is relatively larger for higher injection temperatures.

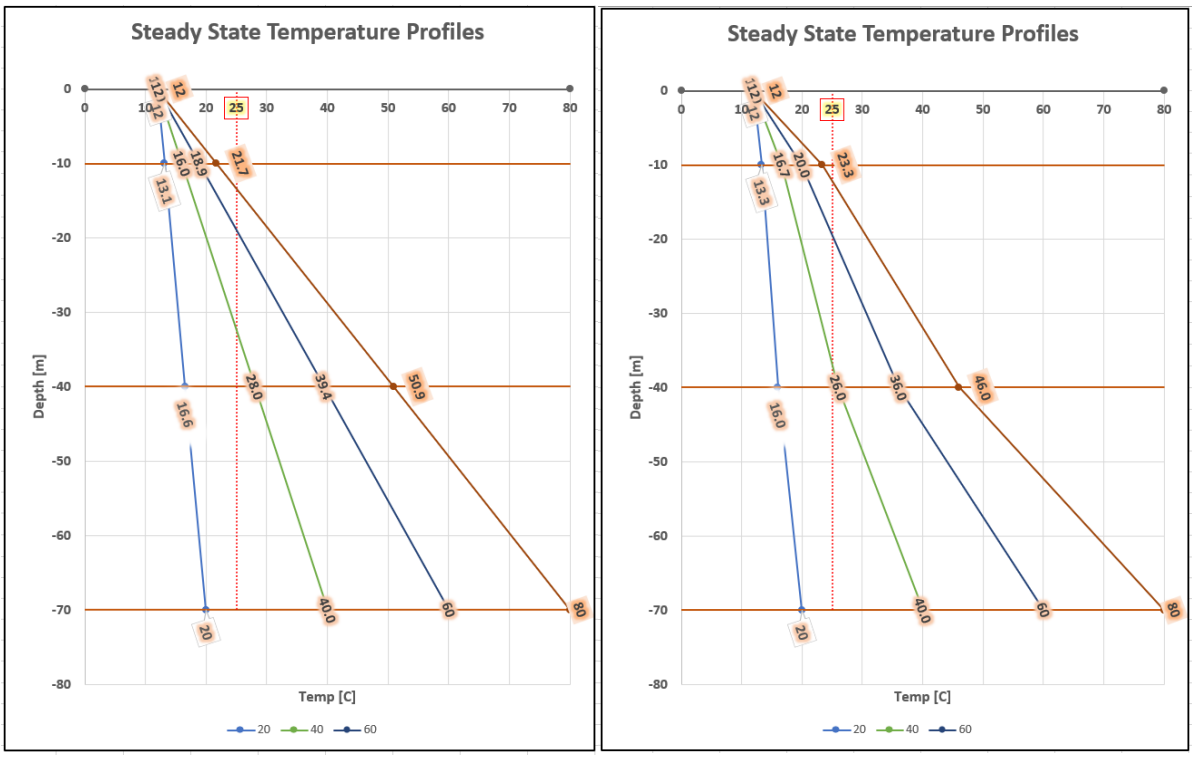

Figure 3.8. Analytical model results for the 1D steady state vertical temperature distribution, for four hot temperature boundaries and the surface as the cold boundary (12°C). horizontal lines indicate tops/bottoms of layers. The upper aquifer reaches from 10-40m depth. a) the bulk thermal conductivities are equal for sand and clay (λ=2.5 W/mK), whereas for b) this value is larger for sand (λ = 3.0) than for clay (λ = 2.5), causing the kink in the temperature distribution.

In this study, the thermal conductivities of sand and clay are equal, so that the 1D vertical steady state temperature distribution is linear in the layers overlying the injection aquifer. In that case, the steady state temperature at the critical depth is only dependent of the temperature differences over the considered overlying soil profile ($T_{bot} - T_{top}$) and the relative distance of the critical depth (D_{crit}) to the hot temperature boundary (H_{cap}/H_{tot}):

$$T_{Dcrit} = \frac{T_{bot} - T_{top}}{H_{tot}} * H_{cap} \qquad \text{(E3.1)}$$

Applying formula E3.1 to the lithology and the temperature boundary conditions of the reference scenarios, the relation between the cap layer thickness and the steady state 1D temperature at the critical depth (D_{crit}) is found for the reference scenarios with the four injection temperatures (see figure 3.9). For larger cap layer thickness (H_{cap}), the distance between D_{crit} and the hot temperature boundary is directly increased and the steady state temperature is decreased. This causes the breakthrough time of a critical temperature (T_{crit}) of 25°C at the critical depth to be longer. Additionally, the steady state temperature can decrease below the critical temperature so that no breakthrough of T_{crit} is expected to occur at all (T_{inj}=40,H_{cap}=60 in figure 3.9).

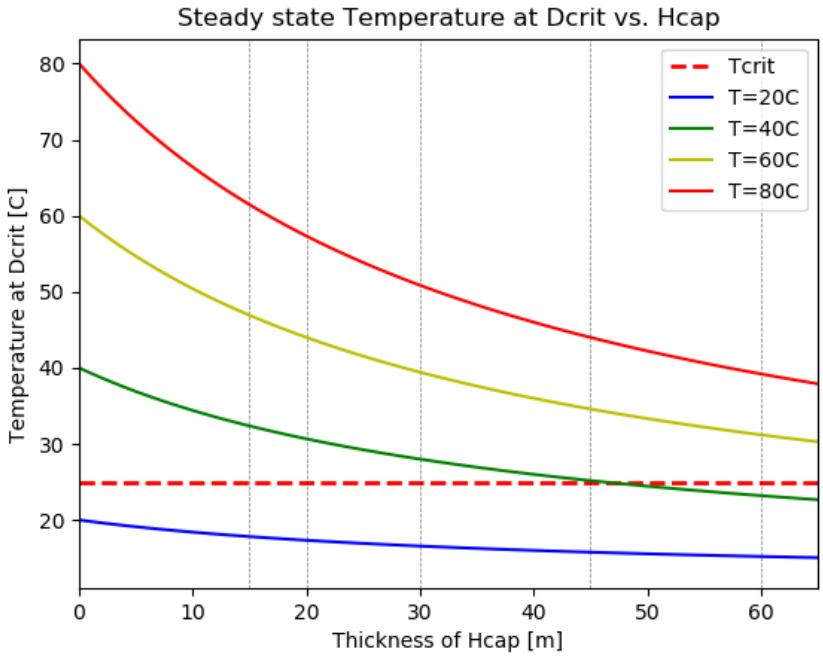

Figure 3.9. Assuming 1D steady state vertical heat conduction, this figure shows the temperature at the critical depth, given the thickness of the separating clay layer and the temperature at the hot temperature boundary. This figure only applies for the lithology used in the reference scenario, with 3 overlying layers: clay(10m), sand(30m), clay (H_{cap} thickness). Critical temperature is dashed.

A simple numerical simulations was performed by the model, where a constant temperature was applied to 70 m depth over the complete model domain. The colder temperature boundary was at the surface (12°C), no flow occurred in the layers and the simulation was run for 100 years. The numerical model resulted in the same long term temperature (after 100 years) as was expected from the analytical 1D steady state heat conduction model.

The top of the injection aquifer in the numerical model moves towards a constant temperature after a long time. These numerically found long term temperatures at the top of the injection aquifer define the constant hot temperature boundaries to be supplied to the analytical model. The analytical model uses this long term temperature as input for the hot temperature boundary, and predicts what temperature is expected at the critical depth on the long run. This temperature can be compared to the numerically modelled temperature at the critical depth to show whether the analytical model accurately predicts the long term temperature that is simulated by the model. The results are shown in Appendix A.1. It was shown that:

- For a given location, when the constant temperature boundary conditions and the thermal properties of the overlying soil profile are provided and accurate, the analytical model provides a good first order approximation of the steady state temperature distribution that is approached on the long term (within 100 years).
- Differences between the analytical and numerical output can be caused by several factors. Firstly, the analytical model assumes that the hot temperature boundary is constant, but in the numerical model it takes time for the upper part of the injection aquifer to develop towards this temperature. This can result in numerical temperatures lower than analytically expected: the system is not yet in thermal equilibrium after 100 years. Also, the analytical model assumes 1D heat conduction, whereas the numerical model is 2D.
- Highest differences between the numerical and analytical model were found for locations further from the well and for scenarios with higher injection temperatures. These differences are

explained by the fact that it takes longer to obtain thermal equilibrium for distant locations, and when a large temperature increase must be overcome to approach thermal equilibrium.

- When density driven flow is induced in the upper aquifer, the vertical 1D temperature distribution is not linear anymore (see figure 3.10c,d). The numerically modelled temperatures at the critical depth were higher than the analytically predicted temperatures for locations close to the well, and lower at larger distance from the well.
- Density driven flow in the upper aquifer occurs at the higher temperature reference scenarios (T≥60°C). It only occurs when the temperature at the bottom of the upper aquifer exceeds 40°C (see fig 3.10c).

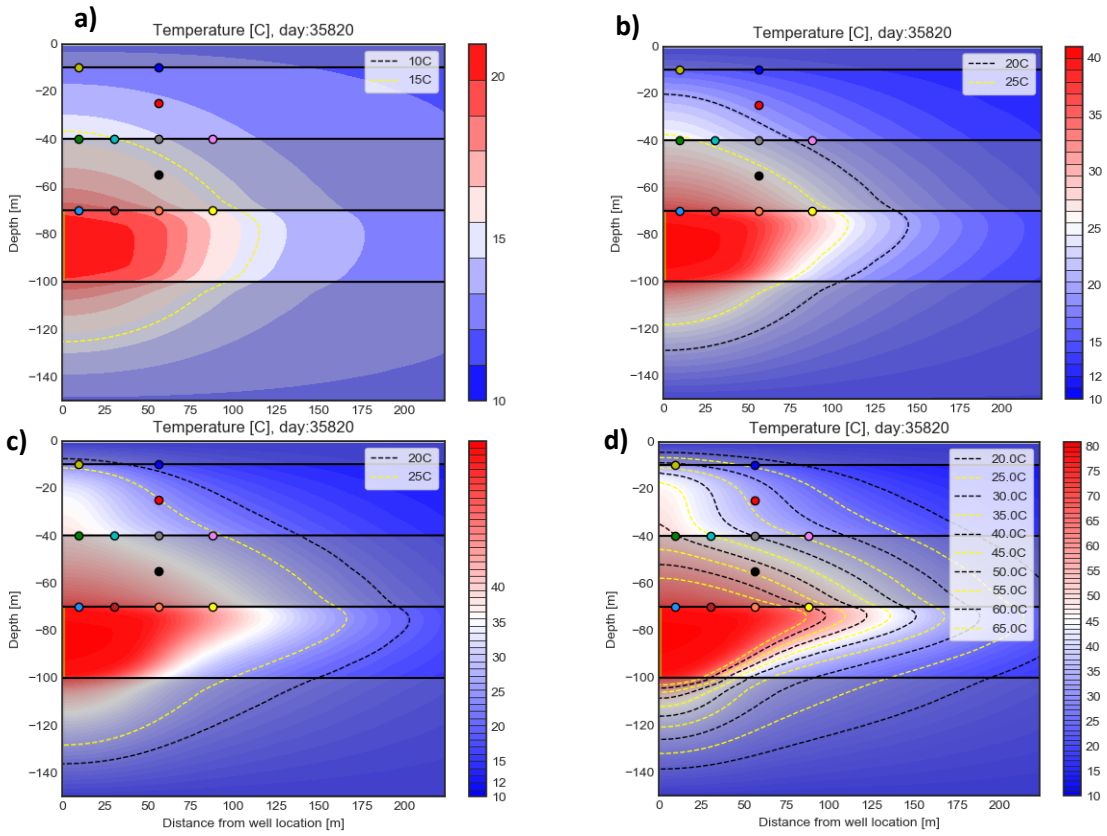

Figure 3.10 vertical cross sections showing the temperature distributions of all temperature scenarios after 100 years. Yellow and black lines indicate isotherms (see legend). Density driven flow only occurs in the T=60 and T=80 scenarios (bottom).

3.2.2 Sensitivity analysis

Twelve observation nodes were used to track temperature changes in space and time in more detail. Figure 3.11 shows their locations and temperature developments for the 100-cycles reference scenario of T_{inj}=80°C. The radial coordinates are constant for all scenarios, but the depths of the lower five points (obs4, obs9-12) depend on the chosen lithology, as these nodes are situated either in the middle or at the bottom of the clay layer whose thickness is changed in some scenarios. Four observation nodes (obs 5-obs8) were allocated to the critical depth D_{crit} (-40m) to register temperatures at this critical location in detail. The main observations were:

- The injection and production of warm water resulted in oscillating temperatures in the injection aquifer. The amplitudes and temperature levels at monitoring points decreased with distance from the well and increased with injection temperature. The clay layer dampens the oscillations, depending on its thickness, so that in and above the clay layer, oscillations were negligible.

- Except for obs1 (golden curve, fig 3.11), temperature curves had a similar shape. When their temperatures start increasing, the rate at which this occurs is high first, but became lower with time. The temperatures moved towards a nearly constant value within 100 years, but after 50 years, the temperatures at the critical depth were already within 10% of the 100th cycle temperature (i.e. approximately steady state).
- The rapid temperature increase at obs1 is caused by density driven flow in the upper aquifer, facilitating flow and transport of heat upwards (see also figure 3.10c-d above). This was only observed for the T=60 and T=80°C scenarios and when the temperature at the critical depth exceeded 40°C.
- An additional model run simulated the T=80°C reference scenario for 200 cycles and showed that temperatures do not significantly change in time after 100 cycles, except within the injection aquifer because of pumping (oscillations). This means that a 2D steady state temperature distribution is obtained in the overlying layers, even when density driven flow occurs in the upper aquifer.

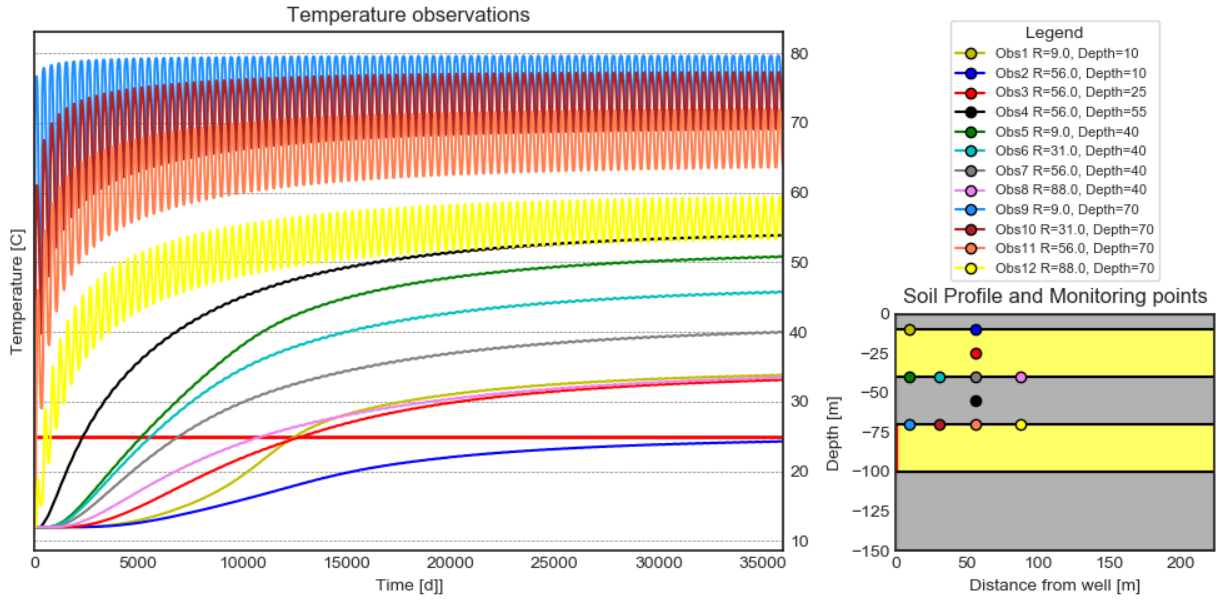

Figure 3.11. temperature observations with time (100 cycles) of the 12 observation nodes. Bottom right: schematic of the modelled soil profile and the locations of the observation nodes. Top right: legend with colors, numbers and radial (R) and depth coordinates of the observation nodes.

The observation nodes have recorded at what time the critical temperature of 25°C (T_{crit}) is measured for the first time. This is referred to as the breakthrough time (BT). A sensitivity analysis was performed to see what parameters dominantly control the breakthrough time of the critical temperature at the critical depth, i.e. at obs5-obs8. When the long-term expected temperatures (according to the analytical model) of a certain location is higher, a shorter breakthrough time of 25°C can be expected. Therefore, the breakthrough time at a given location is related to the long term temperature that can be expected for that location. The breakthrough times at obs5-obs8 are shown in table 3.2. For each scenario (row) the breakthrough time is shown for each injection temperature and each observation node at the critical depth (colors of observation points are in accordance with node colors in figure 3.11 above). Longer/shorter breakthrough times are indicated in green/red. White cells indicate that no breakthrough of T_{crit} was observed within the modelled time. The reference scenario simulated 100 years, all other scenarios 50 years.

Table 3.2. Breakthrough times for the different scenarios simulated. Longer/shorter breakthrough times are indicated in green/red. White cells indicate that no breakthrough of T_{crit} was observed within the modelled time. The reference scenario (REF) simulated 100 year, all other scenarios 50 years.

	Scenario No.	Variation parameter	dfact	BT obs5: R=9m				BT obs6: R=31				BT obs7: R=56				BT obs8: R=88			
				T=20	T=40	T=60	T=80	T=20	T=40	T=60	T=80	T=20	T=40	T=60	T=80	T=20	T=40	T=60	T=80
	REF		1		71.3	21.3	14.3			24.3	15.6			35.0	19.3			86.3	30.3
	0.0	SEAWAT	OFF			29.3	18.5			36.3	22.2				34.1				
Hydrogeological	1.1	H_cap	0.5		14.0	5.6	3.8		20.3	6.9	4.4			10.9	6.1			28.3	11.3
	1.2		0.67		24.4	9.7	6.6		36.3	11.3	7.3			17.2	9.5			41.4	16.5
	1.3		1.5				32.0				34.3				41.2				
	1.4		2																
	2.1	H_inj	0.5			22.1	15.1			25.0	16.3			35.3	20.6				36.2
	2.2		0.67			21.9	14.8			25.0	16.2			36.3	20.3				35.3
	2.3		1.5			20.9	14.1			23.5	15.2			32.2	18.3				26.3
	2.4		2			20.8	14.0			23.4	15.1			31.3	18.2				25.2
	3.1	kv	0.5			22.1	14.6			25.3	16.1			36.5	20.3				32.5
	3.2		2.5			20.8	14.2			23.4	15.3			33.3	18.6				28.5
	3.3		5			20.4	14.2			23.3	15.2			32.5	18.3				28.0
Operational	4.1	Qy	0.5			22.9	14.9			28.3	16.9				23.8				47.3
	4.2		0.67			22.2	14.7			26.3	16.3			43.3	21.4				38.3
	4.3		1.5			20.8	14.2			23.0	15.2			29.9	17.9				25.3
	5.1	well casing	ON			20.2	13.5			23.5	15.3			39.3	20.6				28.4

Breakthrough times of the T=60 and T=80°C scenarios are most occurring and are plotted versus the variation factor of the varied parameters, for obs5-obs8 in figure 3.12. Breakthrough times at obs5-obs8 are most sensitive to the injection temperature and to the thickness of the cap layer. Given an injection temperature, the sensitivity to cap layer thickness is largest. For observations farther from the well (obs8), the breakthrough times decrease with increasing injection volume (Q_y), because the thermal storage gets closer to the observation point. At obs5 and obs6, i.e. close to the well, the injection aquifer thickness has no control on the breakthrough time. Further away, at obs8, increasing the injection aquifer thickness (H_{inj}) decreases the breakthrough time, despite the fact that the thermal radius of the cylindrical thermal volume decreases hence the distance of obs8 to the cylindrical thermal storage increases. The 2D temperature distributions after 50 years for two injection aquifer thickness scenarios provide insight in what happens (figure 3.6). The high injection aquifer thickness scenario shows considerable density driven flow. This causes more residual heat at the top of the aquifer, which in turn results in a radially more extensive thermal impact (i.e. higher long term temperatures) at upper layers compared to the H_{inj}=15m scenario. This gives smaller breakthrough times at the critical depth especially for distant monitoring points. Increasing the vertical hydraulic conductivity (k_V) results in a little decrease of the breakthrough time because buoyancy flow is promoted. When heating from the well casing is considered (Well Casing=ON, sc5.1), the breakthrough times of observation points close to the well (obs5,obs6) were slightly smaller w.r.t. the reference scenario. An additional 100-cycle scenario was performed where the well case heat was applied. Comparing the 2D temperature distribution halfway the 100th cycle with the reference scenario (also 100cycles) shows that long term temperatures are nearly equal at the critical depth, but long term temperatures were slightly higher in the upper aquifer, especially close to the well (see fig 3.13a-b, note the horizontal scale differences). These differences are smaller for lower injection temperatures. Looking to 2D temperature distribution timeframes after 10-20 cycles (not presented) showed that the well case heating causes the isotherms close to the well to move more quickly, so that the long term (steady state) temperature distribution is sooner obtained. So: the temperature distribution is not considerably different when well heating is 'switched on', but it is obtained earlier. Differences in the long term (50th cycle) temperature distributions between the reference scenario and the well case heating scenarios were smaller for smaller injection temperatures. Note that the above observations apply to the modeled scenario range.

Two extra model runs were performed where the specific heat ($C_{p,s}$) and bulk density ρ_{bulk} of the cap layer were individually increased. Increasing either of these parameter increases the thermal retardation. Increasing either the $C_{p,s}$ or the ρ_{bulk} by 20% resulted in a higher thermal retardation coefficient. The simulations showed an increase in the breakthrough times of <10% for obs5-8 and a decrease of the temperatures at obs5-8 after 50 years of <5%. Another additional model run was performed where the thermal conductivity of sand was increased by 20% in the T=80°C reference scenario. This results in a kinked steady state vertical temperature distribution (like fig 3.8b) and shows that after t=50yrs the temperatures at obs5-8 are ±10% lower than the reference scenario. Breakthrough times were increased by 27%, which is more considerable.

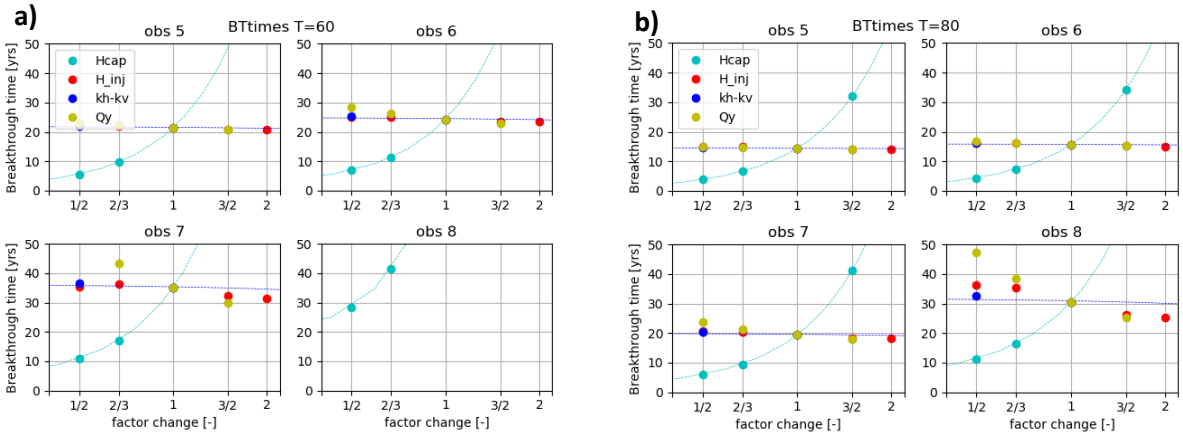

Figure 3.12. Breakthrough times of the critical temperature at obs5-obs8, plotted versus dfact for the scenarios where H_{cap}, H_{inj}, k_V and Q_y are varied. a) injection temperature of 60°C b) injection temperature of 80 °C.

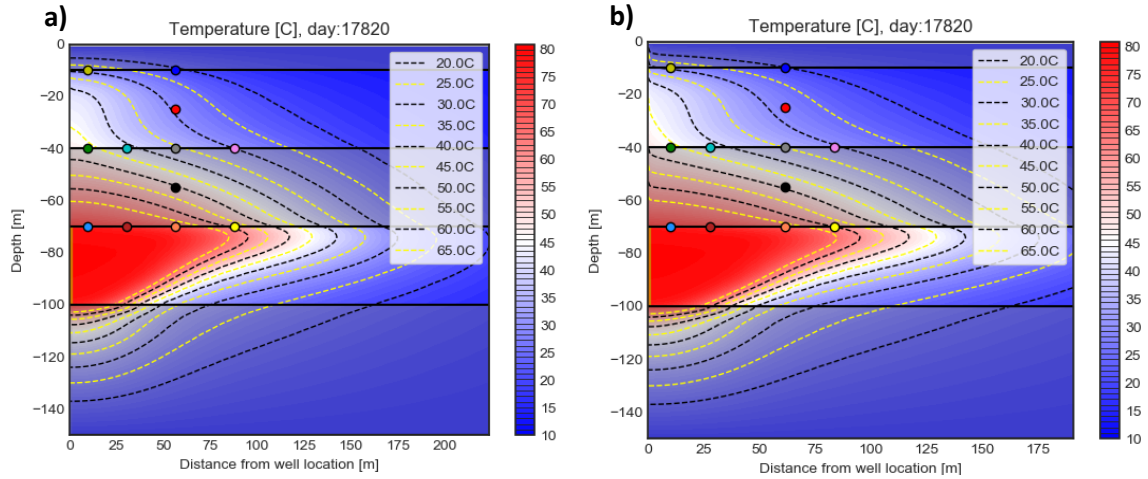

Figure 3.13. 2D temperature distributions halfway the 100th cycle for a T=80°C scenario. a) Reference scenario, b) scenario where well casing heating is applied. Isotherms are indicated in black and yellow. Temperature distributions are similar (note horizontal scale difference).

4 Discussion

4.1 Thermal recovery efficiency

- For the scenarios modelled, the heat transport processes of heat conduction and density driven flow are the dominant processes contributing to thermal energy losses in HT-ATES.
- The recovery efficiency depends on the interplay of temperature and hydrogeological and operational parameters. For low injection temperatures where no or negligible density driven flow occurs within a HT-ATES cycle, the storage shape dominantly controls the conduction losses hence the efficiency. For higher injection temperatures, the temperature difference between the injected and native water defines the instability of the system hence the 'willingness' of density driven flow to occur. The extent to which this is actually allowed within a HT-ATES cycle is dominantly controlled by the injection aquifer thickness (H_{inj}) and the yearly injected volume (Q_y), for the scenarios run in this research. For the simulated scenarios, the efficiency was very sensitive to increasing the injection aquifer thickness when a certain 'critical' value of the injection aquifer thickness was exceeded. This critical value is lower for higher injection temperatures. Increasing yearly injection volume always increases the efficiency, but this trend is stronger for higher injection temperatures. Given the injection temperature, an approximate optimal Q_y/H_{inj} existed for the models simulated, shifting to higher Q_y/H_{inj} values for higher injection temperatures. For all temperature scenarios, an increasing drop in efficiency was observed when Q_y/H_{inj} drops below 10.000 m^2/yr. This value can be used as critical value in the design of HT-ATES systems, at least when the HT-ATES system is within the scenario range of the research.
- Density driven flow occurs mainly at the end of injection/begin of the production period, because the interface is located at a large distance from the well and the forced convection is small relative to the buoyancy flow.
- The large heat losses associated with high injection temperatures cannot only be explained by the increased area of the thermal storage because of the shape change by buoyancy flow. Density driven flow results in tilting of the interface so that upon extraction, cold water is produced at the bottom and hot water is left at the top of the injection aquifer. This adds to losses in recovered heat. Larger H_{Inj} and smaller Q_y result in lower specific well discharge (m3/d/m filter screen), so that forced convection is lower and buoyancy flow is relatively more favorable. This means that the interface is tilted more and a larger volume of cold water is produced at the bottom of the filter screen. Additionally, larger H_{inj} and smaller Q_y result in smaller thermal radii, so that the interface is closer to the well. Upon rotation of the interface, cold water reaches the bottom of the filter screen earlier so that more cold water is produced and thermal recovery efficiency is lower.
- For the scenario range simulated, efficiency was relatively insensitive (ΔEfficiency<5%) to injection temperature for scenarios with L/R_{th} <0.4 and very sensitive (ΔEfficiency>10%) to it for L/R_{th} > 0.6. This shows that a pancake-like shape of the thermal storage (L/R_{th}<0.5) is important for limiting density driven flow and its effects on efficiency when higher injection temperatures are used.
- For the modelled scenarios, the efficiency is practically insensitive to the vertical hydraulic conductivity of the injection aquifer (k_V). A potential explanation is that even in the smallest k_v value scenario, k_v does not limit the buoyancy flow. An extra simulation was performed with both the injection aquifer thickness and vertical hydraulic conductivity increased (H_{inj}=60 and k_v=20) with respect to the reference scenario. The efficiency was compared to a similar scenario, but with lower k_V (H_{inj}=60, k_v=4). It showed that for an injection aquifer thickness of 60m, the 50th cycle efficiency decreases from 63% to 57% when the vertical hydraulic conductivity is increased from k_V=4 to k_V=20 respectively. So for higher aquifer thickness, vertical hydraulic conductivity becomes more important in controlling the efficiency. Buoyancy flow occurs when density differences are sufficient, so only if two water bodies with considerably different temperatures are in contact with

each other. Whereas free convection causes upward movement of heat, heat conduction causes a heat flux from the hot to the cold water body. So even when hot water is moved upwards because colder water gets under it, heat conduction causes heat to move downwards, countering the speed of upward-moving heat. Another explanation can be that thermal retardation slows the upward movement of heat. As this is not incorporated in the theories describing interface tilting by buoyancy flow, the effects of k_V may have been overestimated. Generally, theories may over- or underestimate effects of density driven flow when the relative importance of different parameters is not correctly accounted for.

- Mixed convection ratio M and the characteristic tilting time are indicative for density driven flow, but only in a qualitative sense.
- The thermal recovery efficiency was not sensitive to the thickness of the overlying cap layer thickness for the modelled scenarios. However, a thinner soil profile overlying the injection aquifer results in a larger heat flux from the hot to the cold temperature boundary, according to the steady state heat conduction theory. Absolute losses by heat conduction are hence higher for shallower storage systems.

4.2 Thermal impact on overlying layers

- Numerical simulations showed that the temperature distribution in the overlying soil profile becomes constant on the long term, even when density driven flow occurred in the upper aquifer and when well screen heating occurs.
- It is of interest to find the steady state temperature distribution, in order to see what parts of the overlying soil profile are safe from negative thermal impact of the HT-ATES system.
- The breakthrough times are closely related to the long term temperature at a certain location. The fact that the breakthrough times are most sensitive to H_{cap} and the injection temperature resembles the relevance of the analytical solution, which is also mainly determined by these two parameters.
- The analytical model provides a good first order approximation of the vertical temperature distribution in the overlying layers that can be expected on the long run, provided that the hot and cold boundary conditions values are accurate. Numerical simulations are needed to find the transient temperature distributions.
- When the temperature at the top of the injection aquifer (dependent of the distance from the well) is known, the analytical model indicates whether temperatures at the critical depth may exceed the critical temperature on the long run.
- For the simulated scenarios, the long term vertical temperature distributions between the ground surface and the bottom of the upper aquifer were linear when no density driven flow was induced in the upper aquifer. The temperature at the critical depth is then determined by the thermal gradient over the overlying soil profile and the thickness of the cap layer over the total thickness of the overlying soil profile (H_{cap}/H_{tot}, E3.1). When density driven flow is induced in the upper aquifer however, the vertical temperature distribution is not linear anymore. In such a case, the analytical model underestimates the modelled temperatures at the critical depth for locations close to the well, and overestimates them farther from the well (R>50m). Density driven flow was induced in the upper aquifer when the temperatures at the bottom of the upper aquifer exceeded 40°C.
- When considerable density driven flow occurs in the injection aquifer, the top of the aquifer is heated to a larger radial extent and this results in a larger radial extent of thermal impact at the critical depth as well. The volume of residual warm water after production is hence important for the radial extent of the thermal impact on overlying layers. This means that high heat losses for high injection temperature scenarios can be associated with a larger volume of residual heat after

extraction hence a larger radial thermal impact on overlying layers. In that case, the thermal impact on underlying layers is much smaller.

- The difference in the long term temperature distribution between scenarios with or without well casing heat is small. For relatively low (T≤40°C) and high (T≥60°C) injection temperature scenarios, this difference was only observed within a distance from the well of <10m and <30 m respectively. Although the 'steady state' temperature distributions were nearly the same, this state was obtained earlier for scenarios where well casing heat was included, because the added heat helps moving the system to its thermal equilibrium. The fact that temperature distributions did not change considerably hints that the heat from the well casing can be transported upwards in the zone close to the well and lost through the surface.

4.3 Assumptions

- According to the 2D axisymmetric model, the head distribution is always perfectly symmetric around the well. In reality, regional groundwater flow and pumping activities in both aquifers can occur, so that hydraulic head distribution is not radially symmetric around the well. The model is merely a tool providing insight in the processes playing, than a representation of the hydrogeological situation at the case study.
- It was assumed that no regional groundwater flow occurs in the upper aquifer. When this would happen, the heat conducted to the upper aquifer may be drained by the flowing water and a relatively low temperature can be kept at the top of the clay layer. This means that a large thermal gradient over the clay layer is maintained, which in turn increases the heat flux hence the conductive losses to the layers overlying the injection aquifer. In such a scenario, the thickness of the clay layer controls the efficiency as well.
- Lateral homogeneity in hydraulic conductivity is assumed in the model. A heterogeneous hydraulic conductivity can result in preferential flow paths, dispersing temperatures. The clay layers are assumed to be confining, but in reality some preferential flow paths may exist that facilitate vertical flow.
- A sinusoidal pumping scheme was assumed to represent a typical seasonal course of heat supply and demand. In reality, heat supply and demand can fluctuate in time, depending mainly on the weather. Moreover, pumping rates in the model are constant for each timestep, so that the sinusoidal pumping scheme is not smooth, but stepped (figure 4.1). Both the injection and production period comprise six timesteps. Each injection and production period starts with a pumping rate of 0 m^3/timestep. This means that in each cycle, the thermal storage volume is left to rest for 30 days before injection or production starts. A rest period serves density driven flow and rotation of the interface especially after the injection period, when the interface is located far from the well.
- It was assumed that both the injection water and the native aquifer waters were not saline. In reality, the native water in the injection aquifer is to a more or lesser extent saline and denser, so that density differences are larger.
- A certain set of input parameters was applied to represent the case study. For any model input values that are inaccurate for a given HT-ATES system, the model output will be to a more or lesser extent different from reality. The results, observations and interpretations from this research apply to the simulated scenario range, but not necessarily to situations where other hydrogeological and operational conditions apply.

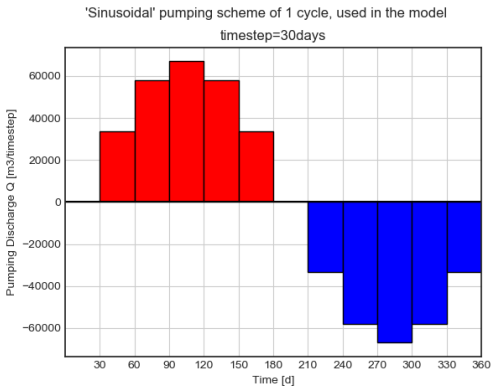

Figure 4.1. Sinusoidal pumping scheme as applied in the simulations. Each block represents one timestep, red/blue colors indicate injection/extraction. There is a 'rest' phase of 1 timestep (30 days) preceding each injection and production phase. Injection and production volumes are equal.

4.4 Research Contribution to HT-ATES system design

The insights obtained from this research can be used for optimizing the design of HT-ATES systems. The process of density driven flow has negative impact on both the thermal recovery efficiency and the thermal impact on overlying layers. For the modelled scenarios with higher injection temperatures, especially large injection aquifer thickness and low yearly injection volumes favored density driven flow. These two parameters need to balance. The Q_y/H_{inj} range for optimal efficiency was 10,000-14,000m^2/yr for injection temperatures of 40-80^oC respectively (fig 3.5). The aquifer thickness cannot be changed by the operator, so the yearly injection volume should be adjusted to get satisfactory thermal recovery efficiencies. For the range of yearly injection volume used in this research (Q_y=125,000-375,000 m^3/yr), injection aquifer thicknesses larger than 30m should be avoided for HT-ATES as increasingly more density driven flow is facilitated upon increasing injection aquifer thickness beyond 30m. However, increasing yearly injection volume increases the radial extent of thermal impact on overlying layers. The optimal HT-ATES system design hence depends on the relative importance of thermal impacts on overlying layers (risk) and the costs associated with losses of recovery efficiency.

Assuming that the reference scenario accurately described the Koppert-Cress HT-ATES system, where injection temperatures of 40^{o}C is applied, the thermal recovery efficiency is not considerably lower compared to a scenario with 20^{o}C injection temperature. No considerable density driven flow was observed within 50 years (fig 3.10b). The analytical model predicts that close to the well, where temperatures are highest, the steady state temperature at the critical depth is 28^{o}C, which is slightly higher than the critical temperature of 25^{o}C. Further away from the well, temperatures are lower and the thermal impact on overlying layer is even lower. Based on this research then, the Koppert-Cress HT-ATES system is not expected to face considerable problems regarding thermal impact on overlying layers and thermal recovery efficiency losses by density driven flow. However, temperature-induced biological and geochemical processes can cause clogging of the well, which in turn affects the overall efficiency of the system. These processes were not considered in this research.

5 Conclusions and recommendations

5.1 Thermal impact on overlying layers

The thermal impact of a high temperature ATES system on overlying layers was assessed by looking at the breakthrough time of a critical temperature of 25^{o}C at the critical depth i.e. the bottom of an aquifer overlying the injection aquifer. Additionally, analytical and numerical model results were assessed to find the temperatures to be expected on the long term at overlying layers. The following insights were derived from the range of scenarios simulated in this research.

- The injection temperature and the thickness of the clay layer between the injection and the upper aquifer are the most important parameters controlling 1) the long-term expected temperatures at the critical depth and 2) the breakthrough time of the critical temperature (25°C) at the critical depth (bottom of overlying aquifer). When for a certain location the expected long term temperature is higher, the breakthrough time of the critical temperature is shorter. For observation nodes at the critical depth further away from the well, the breakthrough times of the critical temperature are also sensitive to the yearly injected volume.
- When density driven flow occurs in the injection aquifer, heat is spread over the top of the injection aquifer and the thermal impact has a larger radial extent on overlying layers, while formations underlying the HT-ATES system are much less affected.
- The 1D steady state analytical model provides a good first order approximation of the vertical temperature distribution that can be expected on the long run at a certain distance from the well. When density driven flow occurs in the upper aquifer, the analytical model underestimates the long term simulated temperatures for locations at the critical depth close to the well and it overestimates them further away from the well.
- The well case heating only affects the long term 3D temperature distribution within a range of 10-30 m from the well. The heating decreases the time needed for the system to obtain the steady state temperature distribution.

5.2 Thermal recovery efficiency

The numerical output also shows to what processes and conditions the thermal recovery efficiency is most sensitive. The main conclusions are listed below and are valid for the range of simulated scenarios.

- This research excludes regional groundwater flow, so that in this study heat losses are dominantly caused by heat conduction and density driven flow.
- Conduction losses cause heat losses in any scenario, but density driven flow-related losses only occur at higher injection temperatures. Their relative contribution depend mainly on the injection temperature, injection aquifer thickness and yearly injection volume. Whereas a flat ('pancake') storage shape negatively affects efficiency for low temperature scenarios because of the relatively high conduction losses, this shape is favorable at higher injection temperatures, because a pancake storage shape limits the extent and the effect of density driven flow, so that the efficiency remains satisfactory.
- In low temperature scenarios, density driven flow losses are negligible and the efficiency is mainly determined by the shape of the thermal storage volume. The thickness of the injection aquifer and the yearly injected volume control the efficiency of the system. Lower A/V ratios give higher efficiencies. For scenarios with injection temperatures ≥ 60°C, considerable heat losses were caused by density driven flow, but the hydrogeological and operational parameters controlled the extent to which this process was facilitated.
- Given an injection temperature ≥ 60°C, efficiency decreases strongly when injection aquifer thicknesses exceed a critical value. This is because the buoyancy flow increases relative to forced convection flow and because the thermal interface is closer to the well so that more cold water is produced, giving lower thermal recovery efficiencies. Buoyancy flow is relatively dominant towards the end of the injection period, when the interface is located far from the well.
- For the scenario range modelled, vertical hydraulic conductivity has negligible control on the efficiency. Explorative simulations showed that this parameter becomes more important when the input parameters are more favorable for density driven flow.

5.3 Recommendations

The conclusions drawn are valid for the range of scenarios modelled in this study. Performance of extra sensitivity analyses with different reference scenarios is needed to obtain a larger framework for evaluation of efficiency and thermal impact of HT-ATES systems. To the author's knowledge, the effects of HT-ATES on overlying aquifers have not been studied in the field, so that validation is not possible. When available, data from existing HT-ATES systems can be studied to see whether the thermal recovery efficiencies are related to the hydrogeological and operational parameters in a similar way as found in this research. When more computational power is available, simulations can be performed on a 3D model domain and with higher temporal resolution, allowing for regional groundwater and/or a combination of pumping wells to be simulated, in more detail. This research used a constant surface temperature, but in reality it changes with time due to the seasons. Adding this to future models may give more accurate predictions of temperature developments in and around HT-ATES systems. The Nusselt number is the ratio of the convective to conductive heat transfer. Rayleigh number describes the heat transfer by buoyancy and viscous forces in free convection. These dimensionless numbers can be used to get more insight in the relative importance heat transfer processes and may be applicable for a larger framework of scenarios.

6 References

Abu-Hamdeh, N. H. (2003). Thermal properties of soils as affected by density and water content. *Biosystems Engineering*, *86*(1), 97–102. https://doi.org/10.1016/S1537-5110(03)00112-0

Bakker, M. (2010). Radial Dupuit interface flow to assess the aquifer storage and recovery potential of saltwater aquifers. *Hydrogeology Journal*, *18*(1), 107–115. https://doi.org/10.1007/s10040-009-0508-1

Bakker, M., Post, V., Langevin, C. D., Hughes, J. D., White, J. T., Starn, J. J., & Fienen, M. N. (2016). Scripting MODFLOW Model Development Using Python and FloPy. *Groundwater*, *54*(5), 733–739. https://doi.org/10.1111/gwat.12413

Bloemendal, M., & Hartog, N. (2018). Analysis of the impact of storage conditions on the thermal recovery efficiency of low-temperature ATES systems. *Geothermics*, *71*(June 2017), 306–319. https://doi.org/10.1016/j.geothermics.2017.10.009

Bloemendal, M., Olsthoorn, T., & Boons, F. (2015). How to achieve optimal and sustainable use of the subsurface for Aquifer Thermal Energy Storage. *Energy Policy*, *66*, 104–114. https://doi.org/10.1016/J.ENPOL.2013.11.034

British Geological Survey. (2011). *Temperature and Thermal Properties*.

Cabeza, L. F. (2015). *Advances in Thermal Energy Storage Systems: Methods and Applications* (Woodheat P). Cambridge: Elsevier.

CE Delft. (2010). *Overzicht van het warmtepotentieel in Nederland: 200-200 in 2020*. Delft.

Chaplin, M. (2017). Physical Anomalies of Water. Retrieved February 21, 2018, from http://www1.lsbu.ac.uk/water/physical_anomalies.html

Diersch, H. J. G., & Kolditz, O. (2002). Variable-density flow and transport in porous media: approaches and challenges. *Advances in Water Resources*, *25*, 899–944. Retrieved from https://ac-els-cdn-com.proxy.library.uu.nl/S0309170802000635/1-s2.0-S0309170802000635-main.pdf?_tid=5d9711f6-e0c0-11e7-ac07-00000aab0f26&acdnat=1513250427_4b1ebd28312f9e58a45b870ed3dde291

Doughty, C., Hellstrom, G., Tsang, C. F., & Claesson, J. (1982). a Dimensionless Parameter Approach To the Thermal-Behavior of an Aquifer Thermal-Energy Storage-System. *Water Resources Research*, *18*(3), 571–587.

DWA. (2016). *Bepalende factoren voor goed functionerende WKO*.

Economische Zaken. (2016). *Rapportage bodemenergiesystemen in Nederland*. Utrecht.

Griebler, C., Brielmann, H., Haberer, C. M., Kaschuba, S., Kellermann, C., Stumpp, C., … Lueders, T. (2016). Potential impacts of geothermal energy use and storage of heat on groundwater quality, biodiversity, and ecosystem processes. *Environmental Earth Sciences*, *75*(20), 1391. https://doi.org/10.1007/s12665-016-6207-z

Guo, W., & Langevin, C. D. (2002). *User's Guide to SEAWAT: A computer program for simulation of three-dimensional variable-density ground-water flow. USGS Techniques of Water Resources Investigations*.

Hamdhan, in, & Clarke, B. (2010). Determination of thermal conductivity of coarse and fine sand soils. *Proceedings of World Geothermal …*, (April), 25–29. Retrieved from http://www.geothermal-energy.org/pdf/IGAstandard/WGC/2010/2952.pdf

Harbaugh, A. W., Banta, E. R., Hill, M. C., & Mcdonald, M. G. (n.d.). MODFLOW-2000, THE U.S. GEOLOGICAL SURVEY MODULAR GROUND-WATER MODEL—USER GUIDE TO MODULARIZATION CONCEPTS AND THE GROUND-WATER FLOW PROCESS. Retrieved from http://wipp.energy.gov/library/cra/2009_cra/references/Others%5CHarbaugh_Banta_Hill_and_McDonald_2000_MODFLOW_2000_Open_File_Report_00_92.pdf

Hellstrom, G., Tsang, C.-F., & Claesson, J. (1988a). Buoyancy Flow at a Two-Fluid Interface in a Porous Medium- Analytical Studie. *Water Resources Research1*, *24*(4), 493–506.

Hellstrom, G., Tsang, C.-F., & Claesson, J. (1988b). Combined Forced-Convection and Buoyancy Flow at a Two-Fluid Interface in a Porous Medium: Analytical Studies. *Water Resources Research*, *24*(September), 507–515.

Hellstrom, G., Tsang, C. F., & Claesson, J. (1979). *Heat storage in aquifers: Buoyancy flow and thermal stratification problems*. Lund, Sweden.

IPCC. (2007). *Climate Change 2007 : An Assessment of the Intergovernmental Panel on Climate Change*. *Change* (Vol. 446). https://doi.org/10.1256/004316502320517344

IPCC. (2014). *Technical Summary*. *Climate Change 2013: The Physical Science Basis. Contribution of Working Group I to the Fifth Assessment Report of the Intergovernmental Panel on Climate Change*. https://doi.org/10.1017/ CBO9781107415324.005

Kim, J., Lee, Y., Yoon, W. S., Jeon, J. S., Koo, M. H., & Keehm, Y. (2010). Numerical modeling of aquifer thermal energy storage system. *Energy*. https://doi.org/10.1016/j.energy.2010.08.029

Kranz, S., & Bartels, J. (2009). Simulation and data based identification of parameters affecting seasonal ATES efficiency. *Effstock 2009*, 1–8.

Langevin, C. D. (2008). Modeling axisymmetric flow and transport. *Ground Water*, *46*(4), 579–590. https://doi.org/10.1111/j.1745-6584.2008.00445.x

Langevin, C. D., Thorne Jr., D. T., Dausman, A. M., Sukop, M. C., & Guo, W. (2007). SEAWAT Version 4: A

Computer Program for Simulation of Multi-Species Solute and Heat Transport. *U.S. Geological Survey Techniques and Methods Book 6*, 39.
Louwyck, A., Vandenbohede, A., Bakker, M., & Lebbe, L. (2014). MODFLOW procedure to simulate axisymmetric flow in radially heterogeneous and layered aquifer systems. *Hydrogeology Journal*, *22*, 1217–1226. https://doi.org/10.1007/s10040-014-1150-0
Omer, A. M. (2008). Energy, environment and sustainable development. *Renewable and Sustainable Energy Reviews*, *12*(9), 2265–2300. https://doi.org/10.1016/j.rser.2007.05.001
Reilly, T., & Harbaugh, A. W. (1993). COMPUTER NOTE: SIMULATION OF CYLINDRICAL FLOW TO A WELL USING THE U.S. GEOLOGICAL SURVEY MODULAR FINITE-DIFFERENCE GROUND-WATER FLOW MODEL. *Ground Water*, *31*(3), 489–494.
RHC. (2013). *Strategic Research and Innovation Agenda for Renewable Heating & Cooling*. Brussels.
Schout, G., Drijver, B., Gutierrez-Neri, M., & Schotting, R. (2014). Analysis of recovery efficiency in high-temperature aquifer thermal energy storage: A Rayleigh-based method. *Hydrogeology Journal*. https://doi.org/10.1007/s10040-013-1050-8
Sommer, W. (2015). Modelling and monitoring of Aquifer Thermal Energy Storage Impacts of heterogeneity, thermal interference and bioremediation. Retrieved from http://edepot.wur.nl/342495
Spakovszky, Z. (2013). *Introduction to Engineering Heat Transfer*. Retrieved from https://ocw.mit.edu/courses/aeronautics-and-astronautics/16-050-thermal-energy-fall-2002/lecture-notes/10_part3.pdf
Staatstoezicht op de Mijnen. (2018). *Advies Groningen-gasveld n.a.v. aardbeving Zeerijp van 8 januari 2018*. Den Haag.
Thorne, D., Langevin, C. D., & Sukop, M. C. (2006). Addition of simultaneous heat and solute transport and variable fluid viscosity to SEAWAT. *Computers and Geosciences*, *32*(10), 1758–1768. https://doi.org/10.1016/j.cageo.2006.04.005
Tsang, C. F., Buscheck, T., & Doughty, C. (1981). Aquifer thermal energy storage: A numerical simulation of Auburn University Field Experiments. *Water Resources Research*, *17*(3), 647–658. https://doi.org/10.1029/WR017i003p00647
UNFCCC. Paris Climate Change Conference-November 2015, COP 21, 21932 Adoption of the Paris Agreement. Proposal by the President. § (2015). https://doi.org/FCCC/CP/2015/L.9/Rev.1
van Bokkum, M. (2018, February 1). Wiebes wil gaswinning “zo snel mogelijk” verlagen tot 12 miljard kuub. *NRC Handelsblad*, pp. 2–3.
van Lopik, J. (2015). *Thermally driven groundwater flow due to heat flux from hot well casings*. Utrecht University.
Vandenbohede, A., Louwyck, A., & Vlamynck, N. (2014). SEAWAT-Based Simulation of Axisymmetric Heat Transport. *Groundwater*, *52*(6), 908–915. https://doi.org/10.1111/gwat.12137
Vewin. (2015). *Dutch drinking water statistics*. *Journal of Chemical Information and Modeling*. The Hague. https://doi.org/10.1017/CBO9781107415324.004
Wagner, W., & Kretzschmar, H.-J. (2008). *International Steam Tables - Properties of Water and Steam* (2nd ed.). Heidelberg: WMXDesign GmbH. Retrieved from https://link-springer-com.proxy.library.uu.nl/content/pdf/10.1007%2F978-3-540-74234-0.pdf
Wallis, I., Prommer, H., Post, V., Vandenbohede, A., & Simmons, C. T. (2013). Simulating MODFLOW-Based Reactive Transport Under Radially Symmetric Flow Conditions. *GroundWater*, *51*(3), 398–413. https://doi.org/10.1111/j.1745-6584.2012.00978.x
Ward, J. D., Simmons, C. T., & Dillon, P. J. (2007). A theoretical analysis of mixed convection in aquifer storage and recovery: How important are density effects? *Journal of Hydrology*, *343*(3–4), 169–186. https://doi.org/10.1016/j.jhydrol.2007.06.011
Ward, J. D., Simmons, C. T., & Dillon, P. J. (2008). Variable-density modelling of multiple-cycle aquifer storage and recovery (ASR): Importance of anisotropy and layered heterogeneity in brackish aquifers. *Journal of Hydrology*, *356*(1–2), 93–105. https://doi.org/10.1016/j.jhydrol.2008.04.012
Ward, J. D., Simmons, C. T., Dillon, P. J., & Pavelic, P. (2009). Integrated assessment of lateral flow, density effects and dispersion in aquifer storage and recovery. *Journal of Hydrology*. https://doi.org/10.1016/j.jhydrol.2009.02.055
Zheng, C., & Wang, P. P. (1999). MT3DMS: A Modular Three-Dimensional Multispecies Transport Model for Simulation of Advection, Dispersion, and Chemical Reactions of Contaminants in Groundwater Systems; Documentation and User’s Guide.
Zuurbier, K. G., Bakker, M., Zaadnoordijk, W. J., & Stuyfzand, P. J. (2013). Identification of potential sites for aquifer storage and recovery (ASR) in coastal areas using ASR performance estimation methods. *Hydrogeology Journal*, *21*(6), 1373–1383. https://doi.org/10.1007/s10040-013-1003-2

7 Appendix

7.1 Analytical model validation

To see whether the 1D steady state analytical model predicts the same temperature distribution as modelled by the numerical model, first a simple scenario was performed with constant temperature boundaries at the top/bottom and constant thermal conductivities of the considered profile. The long term numerically simulated vertical temperature distribution agreed with the analytical 1D steady state model results based on E2.10, showing that the analytical model is valuable in predicting long term temperature distribution in the overlying soil profile, for simple cases. Then, to validate the analytical model applicability to the lithology and the processes applying to this research, the analytically derived vertical temperature distributions are compared to the numerically modelled temperature distributions after t=100 years. To compare the analytical and numerical results properly, equal hydrogeological parameters were applied to either model. The upper constant temperature boundary is equal as well. The lower temperature boundary needed for the analytical model is derived from the numerically simulated temperature after t=100yrs at the top of the injection aquifer (obs 9-12, see fig 3.11). This temperature oscillates because of the pumping activity but the midline of the oscillation after t=100 years is used as input for the analytical model. This was done at four locations with distance 9, 31, 56, 88m from the well (obs9-12), resulting in four analytically derived steady state temperatures at the critical depth. These were compared to the numerically modelled temperatures at the critical depth at the corresponding radii from the well (obs5-8). This method was applied for injection temperatures scenarios of 20, 40, 60 and 80°C. For t=100 years it was expected that the numerical model had practically assumed the expected analytically derived (steady state) temperature distribution. The relative difference of the numerical output with respect to the analytical result was also calculated. Results are shown in table A.1.

Table A.1. validation of analytical model. Red cells indicate the midline average of the oscillation temperatures at the top of the injection aquifer (obs9-12) after 100cycles for the given location. These temperatures are used as input for the analytical model, which calculates the temperature at the critical depth (obs5-obs8). This analytically expected temperature at the critical depth is compared to the numerically derived temperatures after 100 cycles at the critical depth. Differences in temperature increment (with respect to 12°C) of the numerical model and the analytical model are indicated in percentages.

t = 100yrs

INPUT:

Temperatures at top of injection aquifer, from numerical model

radius ->	0	9m		31m		58m		88m	
	well	**obs9**		**obs10**		**obs11**		**obs12**	
T=20	20	19		18.5		17		15.5	
T=40	40	37		35		32		26	
T=60	60	56		54		48		40	
T=80	80	78		72		68		56	

Output (Analytical)

Analytically derived (steady state) temperatures expected at critical depth, based on input

	well					
radius->	**R=0m**	**obs5**	**obs6**	**obs7**	**obs8**	
T=20	16.6	16.0	15.7	14.9	14.0	
T=40	28.0	26.3	25.1	23.4	20.0	
T=60	39.4	37.1	36.0	32.6	28.0	
T=80	50.9	49.7	46.3	44.0	37.1	

Output (Numerical)

Numerically derived (100th cycle) temperatures at observation points,
and difference in temperature increase (w.r.t. 12°C) compared to analytical output

radius->	0	9m		31m		58m		88m	
	well	**obs5**	**%dif**	**obs6**	**%dif**	**obs7**	**%dif**	**obs8**	**%dif**
T=20	no data	15.6	-10%	15.2	-14%	14.8	-2%	13.8	-10%
T=40	no data	25.8	-3%	24.3	-6%	21.8	-14%	18.9	-14%
T=60	no data	38.0	3%	34.5	-6%	30.2	-12%	25.5	-16%
T=80	no data	51.0	3%	46.0	-1%	40.0	-13%	33.0	-16%

For t = 100yrs, all numerical results lie within 16% of the analytically expected temperature increase. At obs5, the numerically modelled temperatures of the T=60 and 80°C scenarios exceed the steady state ones. This only occurs for the higher temperature scenarios and at monitoring points close to the well. Figure 3.10.c and d show that the isotherms in the upper aquifer show a kink. It is expected that this occurs by density driven flow, giving an underestimation of the temperature by the analytical model close to the well. Further away from the well, the analytical model overestimates the long term temperatures from the numerical model at the critical depth.

Figure A.1a shows the analytically (t=100yrs, continuous line) and numerically (t=50, 100yr, dashed lines) derived temperatures at the top of the injection aquifer and at the critical depth for obs8, for the four injection temperature scenarios. The 100th cycle numerical temperature at obs12 (top of injection aquifer, directly below obs8) was used as hot temperature boundary. It shows that the vertical temperature distributions at 88m from the well move towards the analytically expected one. The temperatures were linearly interpolated between the data locations for all temperature scenarios, resulting in a kinked, approximate temperature distribution. Figure A.1b shows more vertical temperature distributions at R=88m in time. It shows that with time, the temperature distribution at a certain distance from the well moves from the initial constant temperature of 12°C (black vertical line) towards the analytically derived (expected) steady state temperature distribution. After 100 cycles, the difference is relatively small. Locations in the injection aquifer that lie farther from the well need more time to obtain a constant (midline) temperature (see fig3.11, obs12). This means that it will also take more time for the overlying observation nodes (e.g. obs8) to obtain thermal equilibrium. For locations closer to the well, the deviations are smaller than in fig A.1b, see table A.1.

Conclusively, the analytically derived steady state temperature distribution gives a good first order approximation of the long term temperatures that are modelled with the numerical model. For higher injection temperatures (60, 80°C), the analytical solution is less accurate. It was found that close to the well, the analytical model underestimates the long term temperature at the critical depth, whereas farther from the well, it overestimates these temperatures.

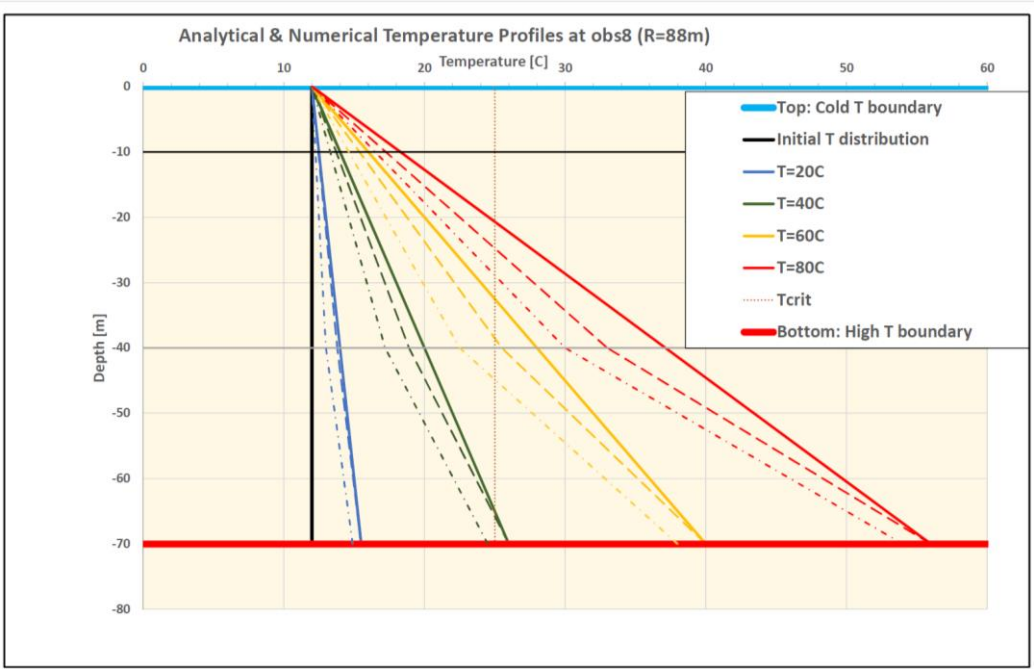

Figure A.1a. Analytical and numerically derived vertical temperature profiles at R=88, for four injection temperatures. Lines: 100 year analytical geotherms. Dashed and dash-dot lines: 100 and 50-year numerical vertical temperature distributions at a distance of 88m from the well.

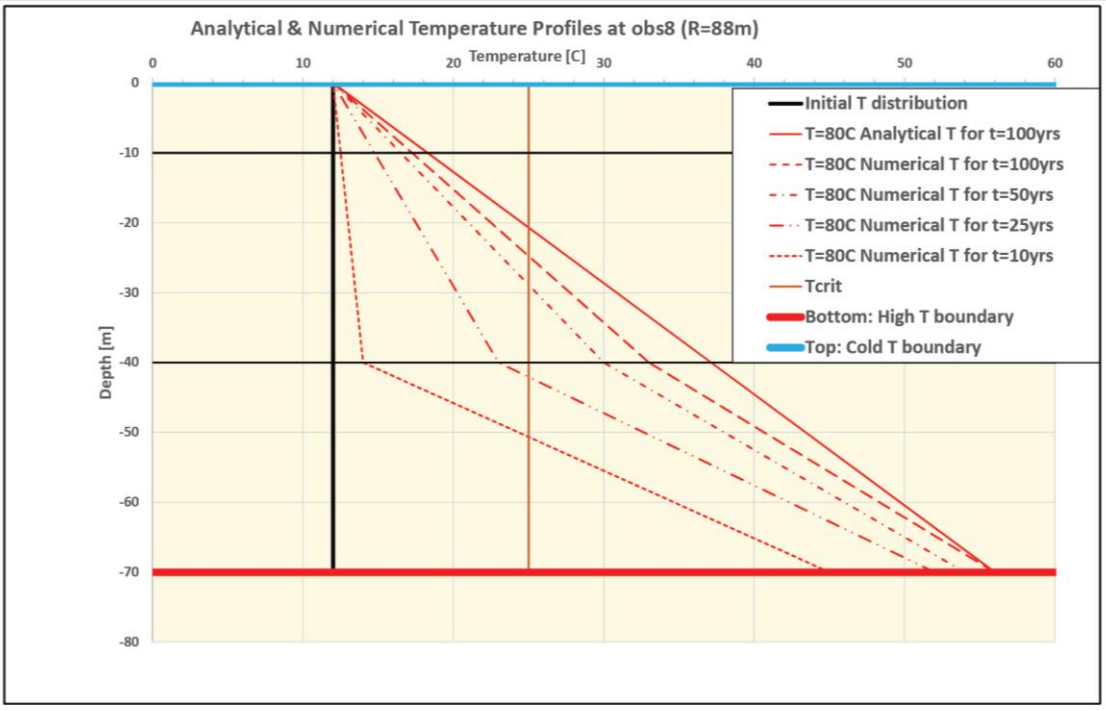

Figure A.1b. The surface temperature is constant (12°C), the numerical temperatures at the critical depth and at the top of the injection aquifer are shown in dashed lines. The analytical model with hot temperature boundary set by the 100 year numerical temperature is shown in a straight continuous line (see legend).